Journal: Bulletin of Engineering Geology and the Environment

Title: A hydromechanical EFG-based Model for Numerical Simulation of Land Subsidence Induced by Groundwater Extraction in Anisotropic Aquifers

Authors: Ahmad Tourei [1,2*], Ali Pak [2], Mohammadali Iranmanesh [3], and Mohammadreza Naddafnia [2]

[1] Department of Geophysics, Colorado School of Mines, Golden, CO, USA
[2] Department of Civil Engineering, Sharif University of Technology, Tehran, Iran
[3] Department of Civil Engineering, K. N. Toosi University of Technology, Tehran, Iran
***** Correspondence: tourei@mines.edu

Abstract: This study presents a coupled hydromechanical element-free Galerkin (EFG) model to simulate land subsidence induced by groundwater withdrawal. The EFG algorithm was validated with unsaturated hydraulic and hydromechanical benchmark problems, showing satisfactory alignment with finite element method (FEM) and theoretical results. We investigated the effects of groundwater pumping on land subsidence and hydraulic head variation in both isotropic and anisotropic aquifers considering unsaturated effects. Our results indicate a nonlinear correlation between groundwater extraction and both hydraulic head decrease and land subsidence increase. In anisotropic aquifers, initial discrepancies were observed between the EFG and FEM models, although final land subsidence and hydraulic head values were closely aligned. Comparison results show that EFG's land subsidence and hydraulic head decline trends for anisotropic aquifer exhibit a better agreement with the isotropic model compared with those of the FEM. The parametric study revealed that the elastic modulus and Poisson's ratio significantly affect land subsidence levels. While hydraulic conductivity influences the rate of hydraulic head decline and onset of subsidence, it has a minor effect on steady-state values. These findings emphasize the importance of accurate in-situ measurements of elastic modulus and Poisson's ratio for the precision and reliability of feasibility studies in groundwater extraction projects.

Keywords: Land subsidence, Groundwater pumping, Coupled hydromechanical modeling, Element-free Galerkin (EFG), Anisotropic aquifers, Unsaturated porous media

1. Introduction

Land subsidence typically results from either a natural disaster, such as earthquakes (Imakiire & Koarai, 2012) or landslides (Tiwari et al., 2020), or human activities, such as the extraction of liquids from subsurface reservoirs (Galloway & Burbey, 2011). As the global population continues to expand, coupled with the rapid growth of industrial and agricultural sectors, there has been a heightened demand for the extraction of groundwater resources. In the last decades, land subsidence caused by groundwater exploitation is considered a worldwide problem (Bonì et al., 2015; Chai et al., 2004; Shirzaei et al., 2021; Wang et al., 2019; Xu et al., 2008), particularly in arid and semi-arid regions (El Kamali et al., 2021; Ghazifard et al., 2016). The Global Hydrological Assessment, conducted by UNESCO in 2013, highlights the significant risk posed to sustainable development by land subsidence resulting from water extraction from aquifers (Asadi & Ataie-Ashtiani, 2015; Donoso, M., Di Baldassarre, G., Boegh, E., Browning, A., Oki, T., Tindimugaya, C., Vairavamoorthy, K., Vrba, J., Zalewski, M., & Zubari, 2012). It is imperative to comprehensively examine the factors influencing land subsidence and devise effective strategies for predicting subsidence levels in aquifers under varying exploitation scenarios to address potential crises adeptly. Groundwater depletion causes narrowing grain gaps and land subsidence. Persistent land subsidence, stemming from changes in pore fluid pressure within solid grain fractures and voids (Amir Hosseini et al., 2023), is presenting a challenge for restoration despite efforts to refill groundwater levels (Fulton, 2006). Global studies underscore the significant contribution of groundwater-level decline to ground surface displacement. Examples such as Las Vegas Valley(Bell et al., 2002), Mexico City(Khorrami et al., 2023), Antelope Valley (Siade et al., 2014), Coastal City of Lagos(Ohenhen & Shirzaei, 2022), Jakarta Metropolitan Area (Abidin et al., 2004), and Mashhad City (Khorrami et al., 2020) emphasize the necessity of scrutinizing land subsidence modeling in research. In certain cases, like Memphis, significant decreases in groundwater levels do not manifest noticeable subsidence, which is potentially attributed to high reservoir density or the presence of rock reservoirs (Poland & Davis, 1969). Studying the mechanical behavior of formations during liquid extraction reveals a nonlinear connection between liquid extraction and regional land subsidence, highlighting the interplay between hydraulic parameters and subsidence and underscoring the importance of numerical modeling in understanding mechanisms affecting land subsidence (Asadizadeh et al., 2022; Motagh et al., 2007; Mousavi et al., 2001).

Due to the challenges associated with studying land subsidence in laboratory settings, various numerical models have been utilized to investigate this phenomenon. Previous studies have modeled land deformation using Finite Element Method (FEM) (Kihm et al., 2007; Kim, 2005; Luo & Zeng, 2011; Yang et al., 2015). Asadi (Asadi & Ataie-Ashtiani, 2015) (2015) developed a theoretical framework combining one-dimensional two-phase and two-dimensional single-phase equations, using the finite volume method to compute settlements in elastic porous media, including saturated and unsaturated layers, focusing on Tehran's subsidence. Rajabi (Rajabi, 2018) (2018) utilized PLAXIS 3D to simulate land subsidence in the Aliabad plain, Iran, considering aquifer pressure variations and employing a theoretical framework based on consolidation theory. Compared to element-based models, meshless methods provide some advantages, including employing higher-order continuity for interpolation, hence attaining precise representation of stress fields, facilitating the modeling of substantial deformations without the possibility of element distortion, and enabling crack propagation simulation (Tey et al., 2020). The element-free Galerkin (EFG) technique (Belytschko et al., 1994) has been employed as a numerical modeling tool for geotechnical problems (Dinesh et al., 2021; Iranmanesh et al., 2018; Iranmanesh & Pak, 2023; Tey et al., 2020; Tourei et al., 2024) and provides a robust framework for addressing complex, nonlinear soil behaviors, offering enhanced accuracy and flexibility compared to traditional finite element methods, especially in simulations involving large deformations and irregular geometries. Pathania et al. (Pathania & Rastogi, 2017) (2017) introduced a novel hydraulic model that uses the meshless EFG technique and the Moving Least Squares (MLS) methodology for simulating groundwater flow in unconfined aquifers, highlighting the advantages of meshless techniques over traditional mesh-dependent methods. This method was validated through simulations in the Blue Lake aquifer, Northern California, and its performance was compared with the MODFLOW software.

EFG is a relatively new type of numerical method that has achieved remarkable success in various hydrological (Park & Leap, 2000; Tey et al., 2020) and geomechanical (Mohammadi, 2006; Varshney et al., 2020) problems. Due to EFG's mesh-free nature, it can offer higher accuracy and convergence by utilizing a higher order of interpolation functions and improves handling of domain discontinuities. Despite the utilization of the EFG method in analyzing multiphase flow in deforming porous media (Samimi & Pak,

2016) or in groundwater modeling studies (Pathania et al., 2019, 2020; Pathania & Rastogi, 2017), application of this technique for coupled hydromechanical modeling in the context of land subsidence in aquifers remains unexplored. This study applies the EFG method to coupled hydromechanical modeling, specifically focusing on land subsidence phenomena and considering unsaturated effects in aquifers. In the subsequent sections, we first provide a brief review of the governing equations for the movement of two immiscible fluids through deforming porous media, followed by discussing the numerical discretization of the model. Subsequently, we use the EFG software to simulate various verification examples. This is then extended to modeling a land subsidence problem, where a parametric analysis is conducted to better understand the effects of various parameters on land subsidence. The proposed numerical model leverages the EFG method to simulate land subsidence and the decrease in hydraulic head, thereby providing a comprehensive understanding of land subsidence due to groundwater extraction.

2. Methodology and Formulation

2.1. Governing Equations for Hydromechanical Modeling of Multiphase Porous Media

A set of equations governing the hydromechanical behavior of a deformable multiphase porous medium includes 1) the linear momentum balance equation for the formation (Equation 1), 2) the linear momentum balance equation (the generalized Darcy's Law) for fluid phases (Equation 2), and 3) the mass balance equation for each fluid phase (Equations 3-4). The integration of mass conservation in the solid phase with that of each fluid phase results in the ultimate form of the continuity equations governing the flow of pore fluids. Assuming constant temperature, full fluid occupancy in the solid skeleton's voids, and minimal interphase mass transfer, the equations for a porous medium with two viscous fluids are stated as follows (Samimi & Pak, 2014, 2016; Thomas, 2000):

$$\sigma_{ij,j} + \rho g_i = 0 \tag{1}$$

$$n\, S_\pi\, \dot{u}_i^{\pi s} = \frac{k_{ij} k_{r\pi}}{\mu_\pi}\left[-p_{\pi,j} + \rho_\pi\right] \qquad \pi = w, nw \tag{2}$$

$$\begin{aligned}\left[S_w \frac{\alpha - n}{K_s}\left(S_w + \frac{\partial S_w}{\partial P_c} P_c\right) + \frac{n S_w}{K_w} - n\frac{\partial S_w}{\partial P_c}\right]\frac{\partial P_w}{\partial t} + \left[S_w \frac{\alpha - n}{K_s}\left(1 - S_w - \frac{\partial S_w}{\partial P_c} P_c\right) + n\frac{\partial S_w}{\partial P_c}\right]\frac{\partial P_{nw}}{\partial t} + \alpha S_w \dot{u}_{i,j} \\ + \frac{1}{\rho_w}\left[\rho_w\, n\, S_w\, \dot{u}_i^{ws}\right]_{,i} = 0\end{aligned} \tag{3}$$

$$\begin{aligned}&\left[(1 - S_w)\frac{\alpha - n}{K_s}\left(S_w + \frac{\partial S_w}{\partial P_c} P_c\right) + n\frac{\partial S_w}{\partial P_c}\right]\frac{\partial P_w}{\partial t} \\ &\quad + \left[(1 - S_w)\frac{\alpha - n}{K_s}\left(1 - S_w - \frac{\partial S_w}{\partial P_c} P_c\right) - n\frac{\partial S_w}{\partial P_c} + \frac{n(1 - S_w)}{K_{nw}}\right]\frac{\partial P_{nw}}{\partial t} + \alpha(1 - S_w)\dot{u}_{i,j} \\ &\quad + \frac{1}{\rho_{nw}}\left[\rho_{nw}\ n\, S_{nw}\, \dot{u}_i^{nws}\right]_{,i} = 0\end{aligned} \tag{4}$$

Equations 1-4 contain various parameters that represent fluid flow characteristics through a porous medium. These parameters include the σ_{ij} tensor of total stress (See Appendix A for generalized Hook's Law), $\rho = (1 - n)\rho_s + n(S_w \rho_w + S_{nw}\rho_{nw})$ average density of the medium, n porosity, ρ_s solid phase density, ρ_π densities of the wetting and non-wetting fluid phases $(\pi = w, nw)$, $\dot{u}_i$ solid phase velocity, S_π fluid phase saturations, μ_π dynamic viscosity, P_π , ρ_π pressure and densities of the flow phases, $k_{r\pi}$ the relative permeability coefficient of the fluid phase, k_{ij} intrinsic permeability tensor (See Appendix B for generalized Darcy's Law), g_i gravitational acceleration vector, α Biot's constant, $P_c = P_{nw} - P_w$ capillary pressure, t time, and K_s, K_π the bulk modulus of the solid phase and fluid phase, respectively. For a hydromechanical study of multiphase systems, the above nonlinear equations need to be supplemented with auxiliary functions, such as saturation degree as a function of capillary pressure, permeability coefficient as a function of saturation degree of wetting and non-wetting phases, and constitutive law of the solid phase (Samimi & Pak, 2016).

To model unsaturated porous media, we considered van Genuchten (van Genuchten, 1980), Brooks-Corey (Brooks & Corey, 1964), and Huyakorn et al. (P.S. HUYAKORN, 2007) equations for the numerical modeling. In Table 1, α, β, and γ are van Genuchten's parameters, p_d is the air-entry pressure for the Brooks-Corey model. and n is the Huyakorn et al.'s parameter.

Table 1 Saturation and permeability equations for unsaturated media

Reference	Normalized saturation ratio	Relative permeability coefficients
van Genuchten (van Genuchten, 1980)	$S_e = \left(1 + (\alpha\, p_c)^\beta\right)^{-\gamma}$	$k_{r_w} = \sqrt{S_e}\left[1 - \left(1 - S_e^{\frac{1}{\gamma}}\right)^\gamma\right]^2$ $k_{r_{nw}} = \sqrt{1 - S_e}\left(1 - S_e^{\frac{1}{\gamma}}\right)^{2\gamma}$

Brooks-Corey (Brooks & Corey, 1964)	$s_e = \left(\frac{p_c}{p_d}\right)^{-\lambda}$	$k_{r_w} = s_e^{\left(\frac{2}{\lambda}\right)+3}$ $k_{r_{nw}} = (1 - s_e)^2 \left(1 - s_e^{\left(\frac{2}{\lambda}\right)+1}\right)$
Huyakorn et al. (P.S. HUYAKORN, 2007)	$S_e = \left(1 + (\alpha\, p_c)^{\beta}\right)^{-\gamma}$	$k_{r_w} = {S_e}^{n}$ $k_{r_{nw}} = (1 - S_e)^{n}$

2.2. Initial and boundary conditions

By considering the soil skeleton displacement (u_i) and fluid pressures (P_w, P_{nw}) the main variables or problem unknowns, necessary initial and boundary conditions for solving the governing equation system can be expressed as follows (Samimi & Pak, 2012, 2016):

- Initial conditions are:

$$u_i = u_i^0, and\ p_\pi = p_\pi^0\ (\pi = w, nw)\ at\ t = 0\ on\ \Omega \tag{5}$$

- Dirichlet boundary conditions are:

$$\begin{aligned} P_\pi &= \bar{P}_\pi \quad on \quad \Gamma_{P_\pi} \\ u_i &= \bar{u}_i \quad on \quad \Gamma_{\mathrm{u}} \end{aligned} \tag{6}$$

- Neumann boundary conditions are:

$$\begin{aligned} &\sigma_{ij} n_j = \bar{t}_i \qquad on\ \ \Gamma_\sigma \\ &\frac{k_{ij} k_{r\pi}}{\mu_\pi}\left(-P_{\pi,j} + \rho_\pi g_j\right) n_i = \bar{q}_\pi \qquad on\ \ \Gamma_{\mathrm{q}_\pi} \end{aligned} \tag{7}$$

where Ω denotes the problem domain, encompassing boundary Γ, n_i denotes the unit outward vector normal to the boundary, and $\bar{u}_i$, $\bar{t}_i$, $\bar{P}_\pi$, and $\bar{q}_\pi$ denote the specified values for displacement, traction, pore pressure, and flux, respectively, on various segments of the boundary. The subsequent conditions govern these specifications:

$$\begin{aligned} &\Gamma_u \cup \Gamma_\sigma = \Gamma \quad and \quad \Gamma_u \cap \Gamma_\sigma = \phi \\ &\Gamma_{p_\pi} \cup \Gamma_{q_\pi} = \Gamma \quad and \quad \Gamma_{p_\pi} \cap \Gamma_{q_\pi} = \phi \end{aligned} \tag{8}$$

2.3. Numerical Discretization

This study utilizes the EFG meshless technique for discretization of the spatial domain. The EFG approach creates shape functions through the Moving Least Squares (MLS) approximation, consisting of two parts: firstly, a non-zero weight function over a limited zone surrounding a node, known as the node's influence domain, and secondly, a basis function, typically in the form of a polynomial. To spatially discretize the governing partial differential equations, it is necessary to define their integral forms. This is achieved by implementing the weighted residual method in conjunction with the Galerkin approach, alongside the use of the penalty method to enforce the essential boundary conditions. EFG shape functions transform the variational formulation into a matrix representation. These functions approximate fundamental variables, such as displacement and pore fluid pressures, at any given time and location. The matrix representation of the governing nonlinear partial differential equations is presented as:

$$\begin{aligned} &(C_{11} + C_u^\alpha)\dot{U} - C_{12}\dot{P}_w - C_{13}\dot{P}_{nw} = \frac{\partial}{\partial t}(F_u + F_u^\alpha) \\ &C_{21}\dot{U} + C_{22}\dot{P}_w + C_{23}\dot{P}_{nw} + \left(K_{22} + K_{pw}^\alpha\right)P_w = \left(F_{pw} + F_{pw}^\alpha\right) \\ &C_{31}\dot{U} + C_{32}\dot{P}_w + C_{33}\dot{P}_{nw} + \left(K_{33} + K_{pnw}^\alpha\right)P_{nw} = \left(F_{pnw} + F_{pnw}^\alpha\right) \end{aligned} \tag{9}$$

where superscript ($\dot{}$) demonstrates the temporal derivative. Each term in Equation 9 is either a matrix or a vector, assembled from the nodal matrices or vectors, and is detailed in Appendix C. Comprehensive derivation of Equation 9 is beyond the scope of this article, and it is thoroughly provided in Samimi and Pak (Samimi & Pak, 2016). The derived system of equations (Equation 9) is discretized in the time domain, adopting a fully implicit approach with the finite difference method (Samimi & Pak, 2014, 2016). The final system of discrete equations for the fully coupled hydromechanical analysis of three-phase porous media consisting of solid grains and two pore fluids is presented in Equation 10:

$$\begin{bmatrix} C_{11}+C_u^{\alpha} & -C_{12} & -C_{13} \\ C_{21} & C_{22}+\Delta t(K_{22}+K_{Pw}^{\alpha}) & C_{23} \\ C_{31} & C_{32} & C_{33}+\Delta t(K_{33}+K_{Pnw}^{\alpha}) \end{bmatrix}^{n+1} \begin{Bmatrix} U \\ P_w \\ P_{nw} \end{Bmatrix}^{n+1} = \begin{bmatrix} C_{11}+C_u^{\alpha} & -C_{12} & -C_{13} \\ C_{21} & C_{22} & C_{23} \\ C_{31} & C_{32} & C_{33} \end{bmatrix}^{n+1} \begin{Bmatrix} U \\ P_w \\ P_{nw} \end{Bmatrix}^{n} + \Delta t \begin{Bmatrix} \frac{\partial}{\partial t}(F_u+F_u^{\alpha}) \\ (F_{Pw}+F_{Pw}^{\alpha}) \\ (F_{Pnw}+F_{Pnw}^{\alpha}) \end{Bmatrix}^{n+1} \tag{10}$$

By solving this system of equations simultaneously, the unknown variables of displacement vector and pore fluid pressures (wetting and non-wetting) will be calculated. Since the elements of the coefficient matrices in this algebraic equation system are dependent on the main unknowns, an iterative process should be utilized to linearize the problem and obtain the final solution within each time step. A fixed-point type (Thomas, 2000) solution scheme is used in this study to solve the system of Equation 10.

3. EFG Software Verification for Three-phase Hydromechanical Modeling

In this section, we evaluate the performance of the developed EFG software for two-phase fluid flow through nondeformable (Samimi & Pak, 2014) and deformable porous media (Samimi & Pak, 2016). First, we solve an infiltration problem for which the semi-analytical solution is available. Then, we solve a consolidation problem for an unsaturated soil column and verify the results with the Finite Element Method (FEM) results reported by two previous studies (Khoei & Mohammadnejad, 2011; Rahman & Lewis, 1999). For numerical simulation of the examples, it's important to choose suitable numerical parameters that stem from the EFG method applied to the governing equations of two-phase fluid flow through deformable soil medium. This is necessary to maintain the precision of the computational results. In this research, we've adopted the recommendations of Oliaei et al. (Oliaei et al., 2009), with certain adjustments, as discussed in Samimi and Pak (Samimi & Pak, 2014, 2016), as the foundational criteria for selecting the EFG parameters.

3.1. Test case 1: Pressure-driven infiltration

To evaluate the EFG model's effectiveness in solving simultaneous two-phase fluid flow in rigid porous media, we model infiltration caused by pressure with the passive air phase assumption for which a semi-analytical solution has been presented by Philip (Philip, 1956). Several authors have utilized this problem to validate their FEM models (Callari & Abati, 2009; Celia & Binning, 1992; Lehmann & Ackerer, 1998). In this example, water flows from a 30-cm height soil column of rigid material with an initial saturation level of 0.298, corresponding to an initial –100 kPa pore water pressure and 0 air pressure at all nodes. The geometry of this problem is illustrated in Figure 1. The lateral boundaries are impermeable, and both the top and bottom boundaries are permeable with constant pressure of -7.5 kPa and -100 kPa, respectively. Furthermore, the problem considers gravitational acceleration, set as $9.81\left({}^{m}/{}_{s^2}\right)$. The van Genuchten (van Genuchten, 1980) equation is employed to determine suction and relative permeability coefficient. Table 2 includes the model's parameters and the soil's characteristics.

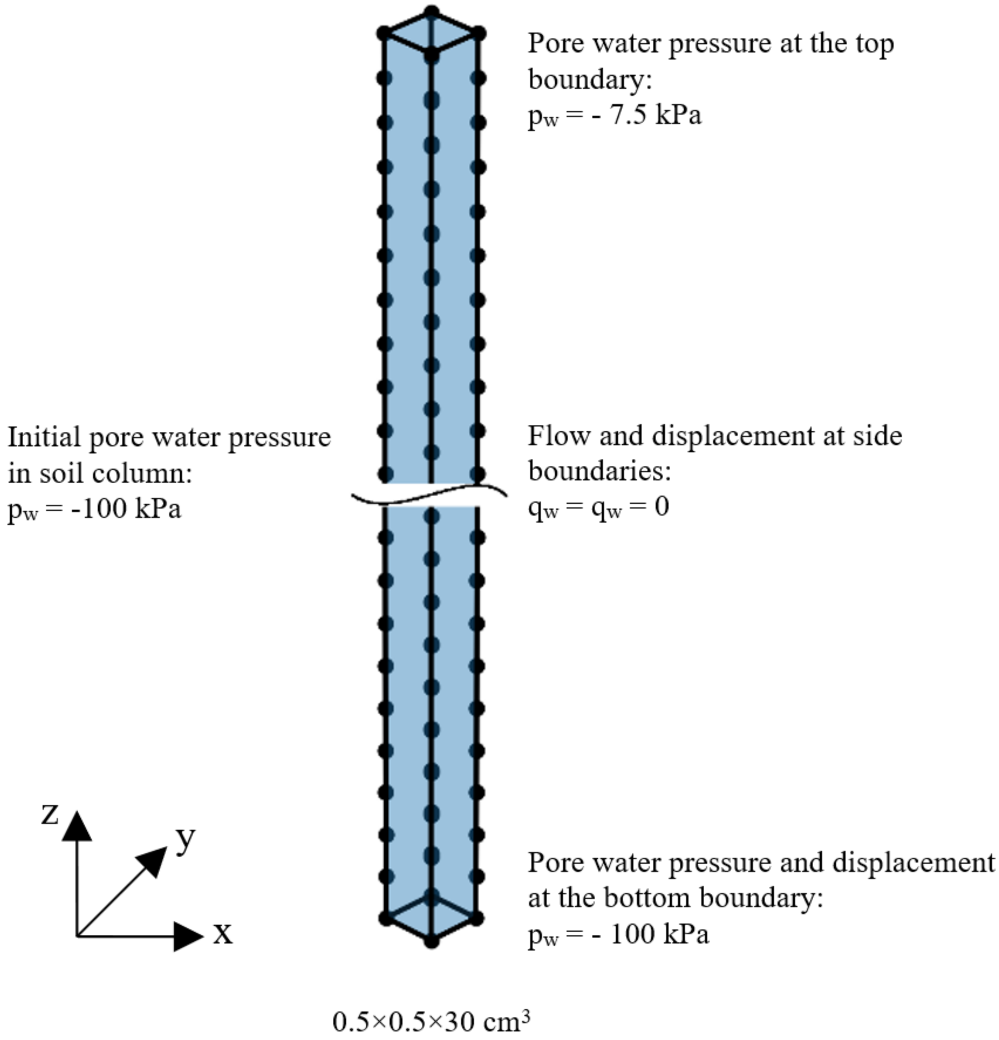

Fig 1 Geometry and initial conditions for test case 1

Table 2 Material properties in test case 1

Properties	**Symbol**	**Value**	**Unit**
Porosity	n	0.368	-
Wetting fluid density	ρ_w	1000	$\frac{Kg}{m^3}$
Non-wetting fluid density	ρ_{nw}	1.22	$\frac{Kg}{m^3}$
Bulk modulus of solid particles	K_s	1.4×10^9	Pa
Bulk modulus of the wetting fluid	K_w	4.3×10^{12}	Pa
Bulk modulus of the non-wetting fluid	K_{nw}	10^{-5}	Pa
Dynamic viscosity of the wetting fluid	μ_w	10^{-3}	$Pa.s$
Dynamic viscosity of the non-wetting fluid	μ_{nw}	10^{-3}	$Pa.s$
Residual saturation	S_{w_r}	0.3966	-
Air entry pressure	P_d	2.25×10^5	Pa
Pore size distribution index	λ	3	-

The spatial discretization of the problem utilizes 244 nodes, featuring a uniform node spacing of 5 millimeters. This includes 61 nodes in the z-direction and 2 nodes each in the x and y-directions. The temporal discretization begins with initial time intervals of 1 second, followed by intervals of 100 seconds. The water pressure profile and saturation degree simulated in different analysis periods are plotted in Figures 2 and 3, respectively. Results are compared with Philip's (Philip, 1956) semi-analytical solution and the FEM model by Callari and Abati (Callari & Abati, 2009). The good agreement between these results indicates a satisfactory performance of the two-phase flow EFG model.

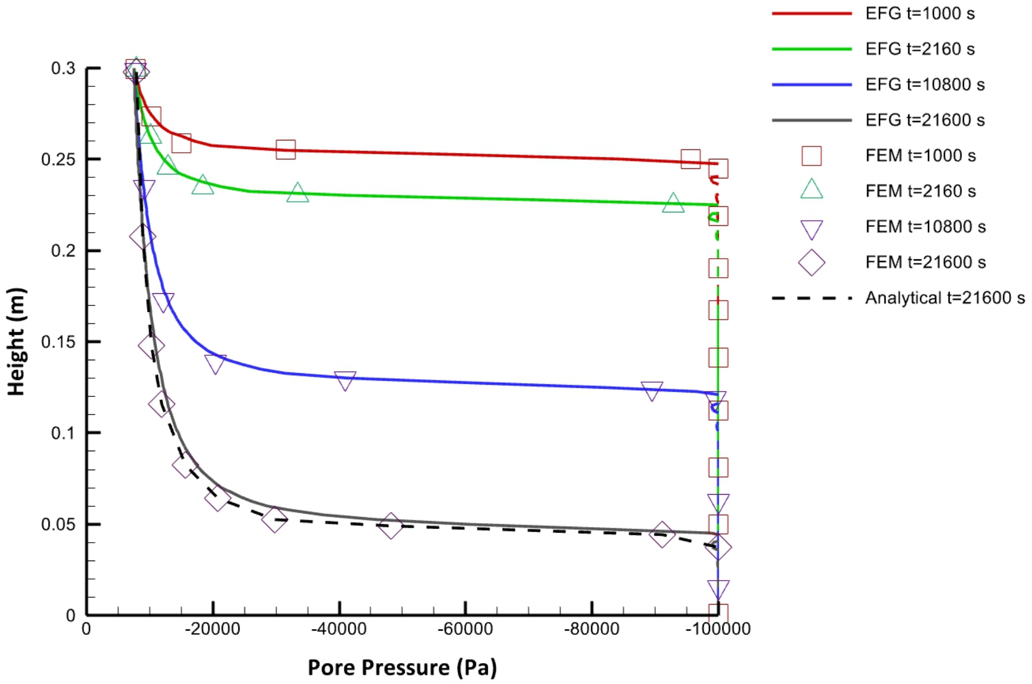

Fig 2 Pore water pressure variation along the soil column over time

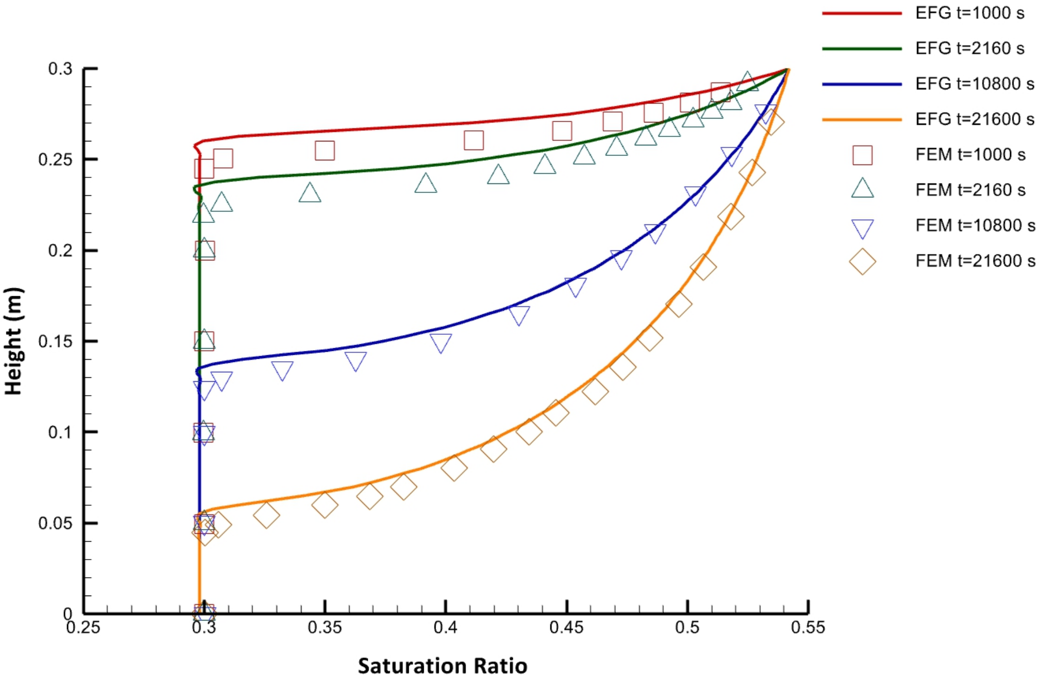

Fig 3. Saturation degree variation along the soil column

3.2. Test case 2: Consolidation of a partially saturated soil column due to evaporation

This example illustrates the behavior of unsaturated soil systems in response to environmental changes. Here, we consider a vertical soil column (Figure 4), composed of linear elastic material measuring 100 cm in height. This column is subject to a surface load of 1 kP at the top boundary. Initially, the soil column is not fully saturated, exhibiting a water saturation level of 0.52. Then, the absolute pore water pressure suddenly decreases to -420 kPa at the top surface, consolidating the soil skeleton. The lateral and bottom boundaries are impermeable, but the upper boundary is permeable. The absolute air pressure at the top surface is 0 kPa. The lateral boundaries are allowed to deform only along the vertical direction, and the bottom boundary is restrained against all displacements. Considering the Brooks and Corey (Brooks & Corey, 1964) equations outlined in subsection 2.1 and based on Rahman and Lewis's study (Rahman & Lewis, 1999), the properties presented in Table 2 are utilized for the numerical modeling of this example.

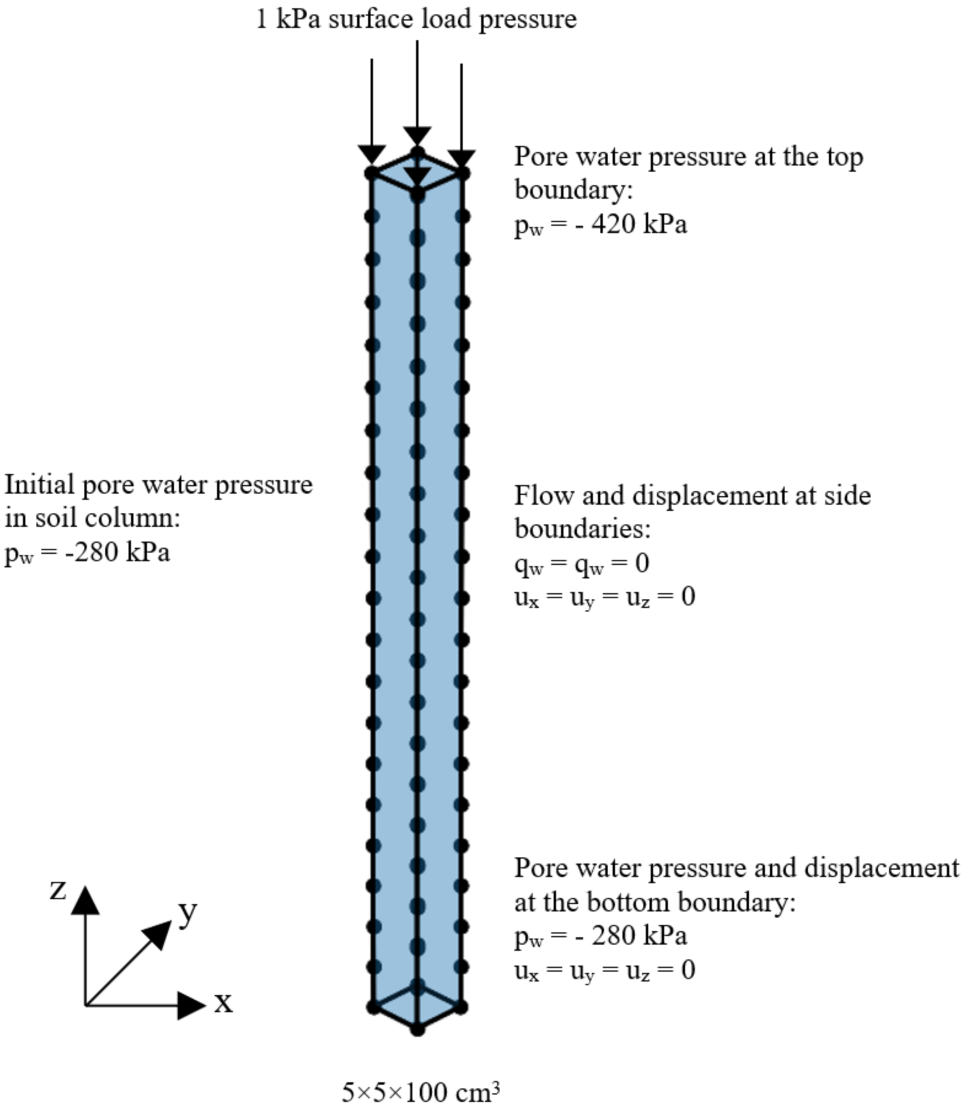

Fig 4 Geometry and initial conditions in test case 2

Table 3 Material properties in test case 2

Properties	**Symbol**	**Value**	**Unit**
Porosity	n	0.368	-
Young modulus	E	6×10^6	Pa
Intrinsic permeability	k	4.6×10^{-12}	m^2
Poisson ratio	υ	0.4	-
Rock density	ρ_s	2000	$\frac{Kg}{m^3}$
Wetting fluid density	ρ_w	1000	$\frac{Kg}{m^3}$
Non-wetting fluid density	ρ_{nw}	1.22	$\frac{Kg}{m^3}$
Bulk modulus of solid particles	K_s	1.4×10^9	Pa

Bulk modulus of the wetting fluid	K_w	4.3×10^{12}	Pa
Bulk modulus of the non-wetting fluid	K_{nw}	10^{-5}	Pa
Viscosity of the wetting fluid	μ_w	10^{-3}	$Pa.s$
Viscosity of the non-wetting fluid	μ_{nw}	10^{-3}	$Pa.s$
Residual saturation	S_{w_r}	0.3966	-
Air entry pressure	P_d	2.25×10^5	Pa
Pore size distribution index	λ	3	-

To model this problem, the spatial domain is uniformly discretized using 21 nodes along the z direction and 2 nodes along both x and y dimensions, resulting in 84 nodes spaced 2.5 cm apart along three dimensions. An initial set of 1-second time steps is adopted due to the higher rate of variation in pore pressure and displacement at the beginning of the simulation, followed by subsequent intervals of 10^2, 10^3 and 10^4 seconds time steps. The vertical displacement profiles and water saturation levels at four different heights within the soil column are shown in Figures 5 and 6, respectively. We observe that soil consolidation lasts approximately six days, after which the soil saturation level reaches the steady state. We compare the displacement and saturation degree results from our EFG model with two previous FEM studies by Rahman and Lewis (Rahman & Lewis, 1999) and Khoei and Mohammadnejad (Khoei & Mohammadnejad, 2011). Based on the results, although there are noticeable variations between the developed EFG and FEM approaches in terms of the spatial and temporal discretization methods, iterative scheme, and formulation used, the EFG model's predictions are in strong agreement with those produced by the other two FEM numerical algorithms. This agreement indicates that the model performance is satisfactory for hydromechanical modeling of two-phase flow problems in deformable porous media.

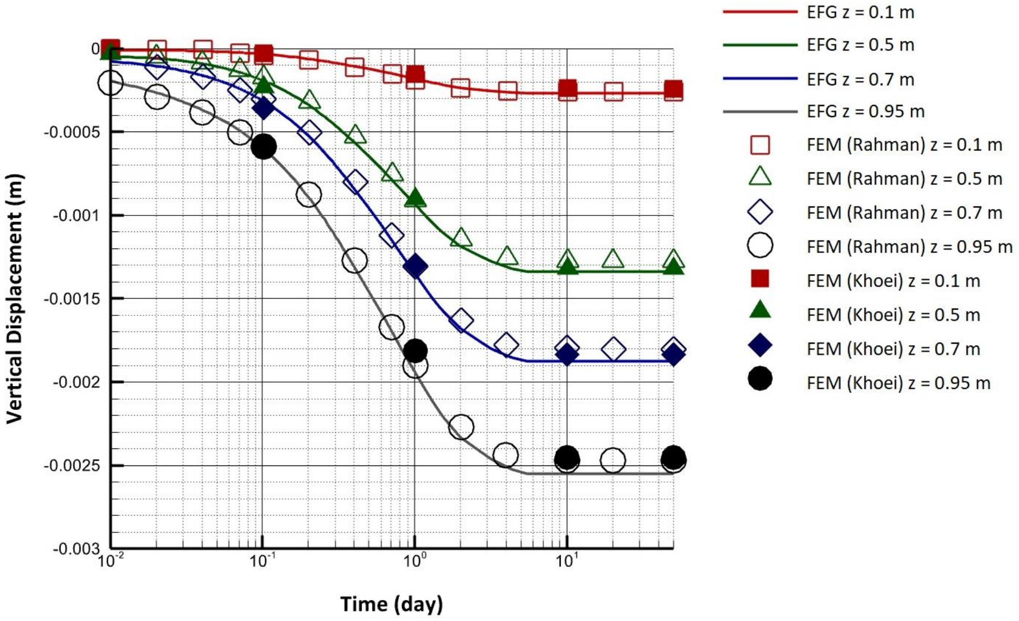

Fig 5 Soil settlement over time during consolidation

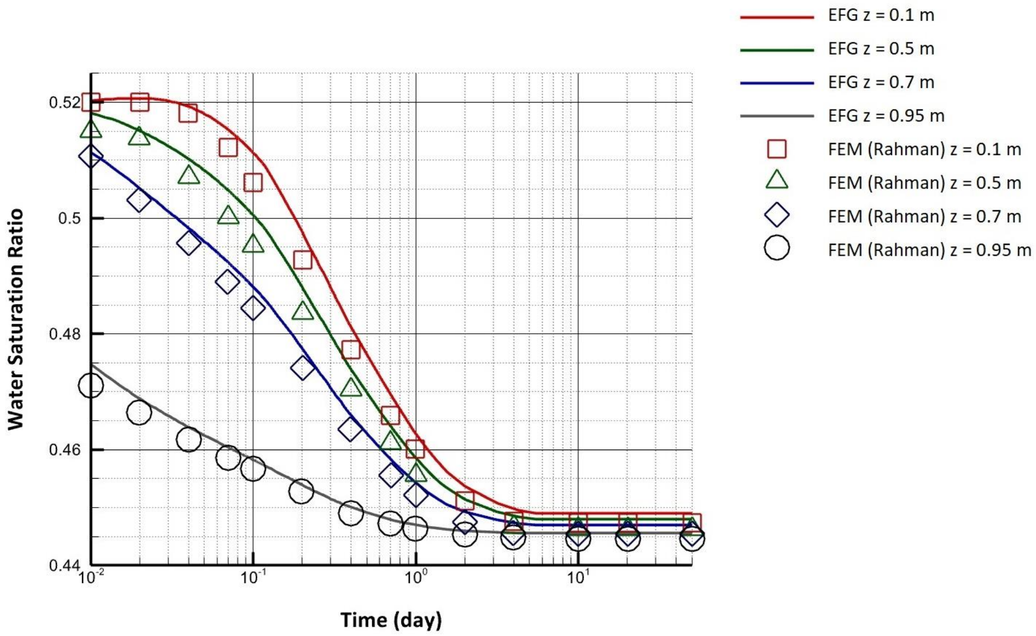

Fig 6 Water saturation variation over time during consolidation

4. Application of the EFG method in land subsidence modeling

4.1. Characteristics of Isotropic and Anisotropic Aquifers

After verifying the EFG software for hydraulic and hydromechanical problems, we investigate land subsidence induced by groundwater withdrawal, considering the unsaturated effects. Our model builds on the foundational work of Kim (Kim, 2005), who used the hydromechanical COWADE 123D software based on finite element techniques. We consider an unsaturated anisotropic soil aquifer, which has a thickness of 50 meters, is characterized by its layered or stratified composition, and is located beneath a landfill site. To reduce the water table elevation below the landfill's base, a fully penetrating pumping well has been installed vertically at the center of the site. The water level in the pumping well is then lowered suddenly to 20 m above the bottom of the aquifer, and this water level is maintained thereafter by controlling the groundwater pumping rate. Following dimensional analysis, lateral boundaries were established 200 meters from the pumping well. Due to lateral symmetry along the x and y axes and to reduce computational cost, our model focused on one-fourth of the designated area. Figure 7 presents the schematic 3D layout of the model, illustrating the specific arrangement of nodes used in the study. For spatial discretization, 2,646 nodes were employed, with a nodal spacing of 10 meters in the x, y, and z directions. This specific number of nodes was determined through various experimental iterations. We observed that if the nodal distance exceeded this threshold, the values at the nodes failed to converge. On the other hand, increasing the number of nodes beyond this point would lead to an increase in computational cost. Figure 8 depicts the y-z plane view of the model at x = 200 m, which illustrates the locations of DO (for subsidence) and HO (for hydraulic head) observation points.

The water table is initially located 45 m above the bottom of the aquifer, making the top 5 meters of the aquifer unsaturated. A negative hydrostatic pore water pressure for the top 0-5 meters and a positive hydrostatic pore water pressure for the deeper 5–45 meters were considered. We assumed the air pressure within the aquifer's pores to be at atmospheric level, typically considered zero. The aquifer lies above a layer of impenetrable rigid bedrock. We assumed that the top boundary of the aquifer is permeable. For rainfall data, we used meteorological data from Seoul, South Korea (Kim, 2005), which indicated an annual rainfall of 1,539 millimeters. Additionally, we assumed the top boundary of the model to be free to move both vertically and horizontally. The model's lateral boundaries are treated as impermeable, with no movement allowed in the direction perpendicular to their plane. The pump is presumed to be within the casing, confining its movement along the x and y axes. Before starting groundwater pumping, the aquifer is at hydrostatic equilibrium condition corresponding to the initial water table location at 45 meters from the bedrock. Therefore, the initial hydraulic head (the summation of hydraulic pressure and elevation head) equals 45 m at all nodes. To account for unsaturated conditions within the top 5 meters of the aquifer (above the initial water table), we use the saturation degree and relative permeability coefficient relationships proposed by Huyakorn et al. (Hu et al., 2019). These relationships are outlined in Table 1. To simulate water pumping, a constant hydraulic head of 20 meters is applied to the pump, spanning from 0 to 20 meters in height.

In this study, we model the aquifer by considering both isotropic and anisotropic conditions. The parameters and properties of the aquifer are given in Table 4 (Kim, 2005). In an isotropic aquifer, the aquifer's parameters, such as hydraulic conductivity, elastic modulus, and Poisson's ratio, are equal in the x, y, and z directions. However, for an anisotropic aquifer, these parameters differ between the horizontal direction and the vertical direction. In the model, we assume soil material is elastic. The generalized formulation of Hooke's Law for derivation of the global elastic modulus tensor, and global saturated hydraulic conductivity tensor is presented in appendices A and B, respectively. The compressibility and specific weight of water are assumed 4.4×10^{10} $\left({m^2}/{N}\right)$ and $9.81\left({kN}/{m^3}\right)$, respectively. Furthermore, the convergence criteria for pressure head and displacements are set equal to 10^{-4} for nonlinear iterations. The total time spanned approximately 10 years. This extended duration was deliberately selected to ensure the aquifers reach an ultimate steady state in the numerical simulations.

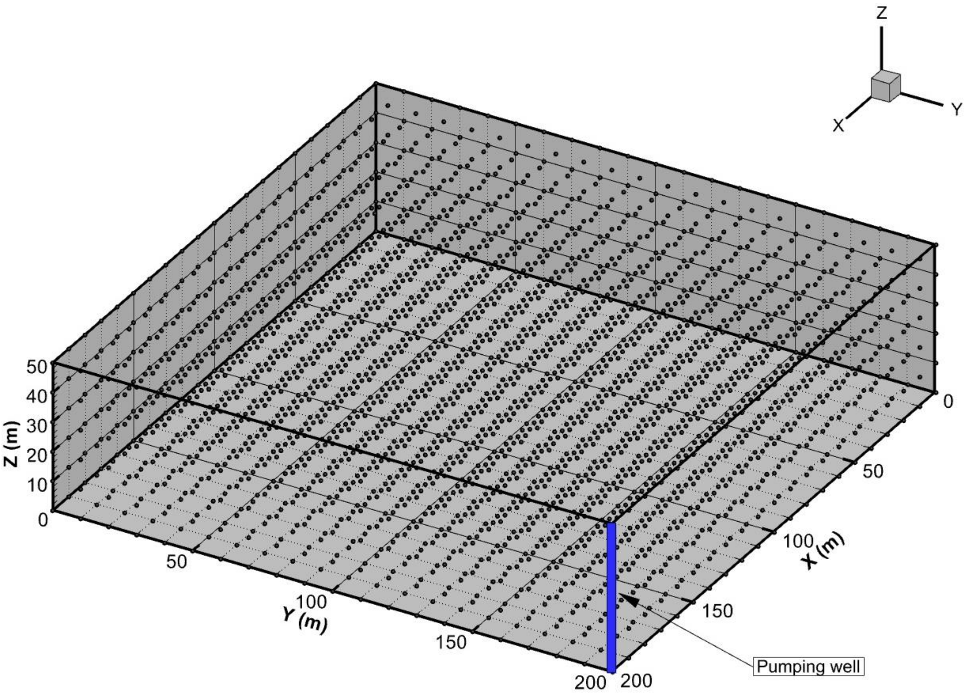

Fig 7 Three-dimensional domain and the nodal arrangement pattern used for the aquifer (beneath the landfill)

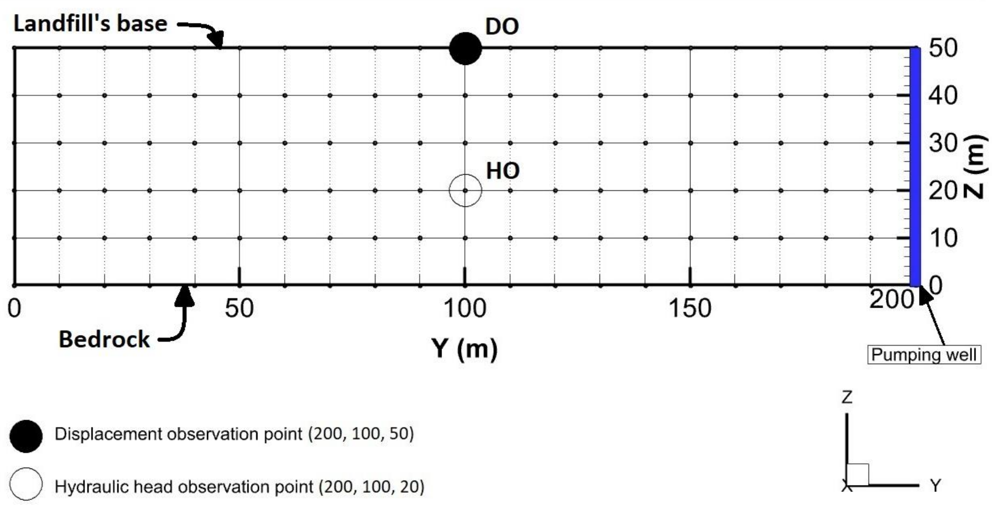

Fig 8 Observing points on the Y-Z plane of the model

Table 4 Characteristics of isotropic and anisotropic aquifers

Property	**Symbol**	**Isotropic Aquifer**	**Anisotropic Aquifer**	**Unit**
Porosity	n	0.25	0.25	-
Elastic modulus				
- Horizontal	$E_x = E_y$	1.47×10^7	2.51×10^7	Pa
- Vertical	E_z	1.47×10^7	5.03×10^6	Pa
Elastic modulus of solid phase	E_s	1.47×10^9	1.47×10^9	Pa
Shear modulus				
- Horizontal	$G_x = G_y$	5.88×10^6	1.16×10^7	Pa
- Vertical	G_z	5.88×10^6	4.19×10^6	Pa
Permeability				
- Horizontal	$K_{sat\,xx} = K_{sat\,yy}$	3.65×10^{-5}	6.42×10^{-5}	$\frac{m}{s}$
- Vertical	$K_{sat\,zz}$	3.65×10^{-5}	1.25×10^{-5}	$\frac{m}{s}$
Poisson ratio				
- Horizontal	v_{xy}	0.25	0.085	-
- Vertical	$v_x = v_y$	0.25	0.427	-
Poisson ratio of solid phase	v_s	0.25	0.25	-
Rock density	ρ_s	2.65×10^3	2.65×10^3	$\frac{Kg}{m^3}$
Residual saturation	S_{w_r}	0.05	0.05	-
Air entry pressure head	h_a	0.0	0.0	m
α parameter for the HUYAKORN model	α_{BV}	0.5	0.5	m^{-1}
β parameter for the HUYAKORN model	β_{BV}	0.2	0.2	-
γ parameter for the HUYAKORN model	γ_{BV}	0.1	0.1	-
n parameter for the HUYAKORN model	n_{BV}	0.2	0.2	-

4.2. Numerical Study Results

Figure 9 illustrates the time-dependent fluctuation of the hydraulic head for isotropic and anisotropic aquifers at the observation point HO, located at coordinates (200, 100, 20) and 100 meters from the pumping well. We compare our EFG results with FEM results reported by Kim (Kim, 2005) to compare numerical results for modeling land subsidence in this aquifer. In both isotropic and anisotropic aquifers, a similar trend is evident when comparing the EFG and FEM techniques. For the anisotropic aquifer, a smaller hydraulic head drop is observed for EFG at the beginning of pumping. EFG resulted in a 0.4 m hydraulic head decrease after 1 hour of pumping. However, FEM resulted in a 1.5 m hydraulic head decrease, approximately 50% of the total hydraulic head drop after about 2000 hours in the steady state. In comparing isotropic and anisotropic conditions, the anisotropic aquifer exhibits a more significant hydraulic head drop, attributable to its higher horizontal hydraulic conductivity and overall higher average horizontal and vertical hydraulic conductivities relative to the isotropic aquifer. However, EFG and FEM results for both isotropic and anisotropic aquifers converge markedly in steady state condition.

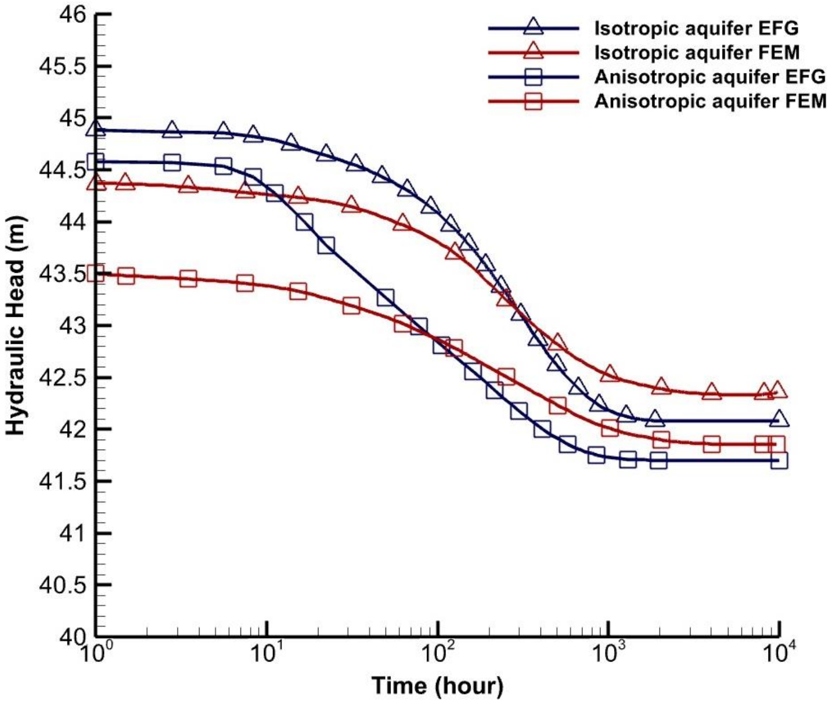

Fig 9 Hydraulic head decrease at point HO over time in the isotropic and anisotropic aquifers

The land subsidence results at observation point DO, located at coordinates (200,100,50), demonstrate a high level of agreement for an isotropic aquifer when comparing the EFG and FEM results, as shown in Figure 10. A land subsidence of approximately 4 cm is observed for both EFG and FEM. However, for the anisotropic aquifer, although EFG and FEM models show a similar trend in land subsidence, there is a shift in early pumping hours. FEM results in a 9 cm of land subsidence after 1 hour of pumping, while the results are 1 cm for EFG models. Similar to the hydraulic head results, the FEM model shows that approximately 50% of land subsidence relative to the total land subsidence in steady state occurs in the first hour of water pumping. This contrasts with the isotropic model, where changes in vertical displacement start after 6 hours of water pumping. EFG results indicate that vertical displacement in the anisotropic model starts after roughly 4 hours of pumping, which aligns more closely with the isotropic model compared to the FEM model. This discrepancy underscores the need for further investigation, which should include verification of models from other sites with field data, to enhance our understanding. The ultimate steady-state land subsidence results for both models converge, and they are greater than the isotropic aquifer's vertical displacement as the vertical elastic modulus for the anisotropic aquifer is smaller than the isotropic aquifer.

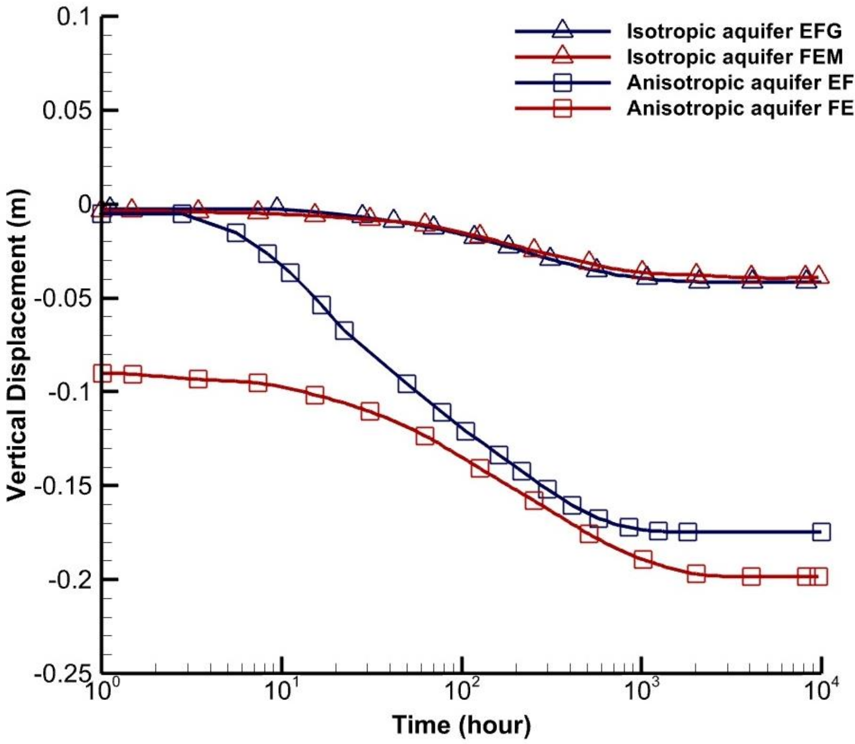

Fig 10 Land subsidence at point DO over time in the isotropic and anisotropic aquifers

Figure 11 illustrates water level variations for the isotropic aquifer, observed at various distances from the pumping well and over different time intervals (1, 10, 100, 1000, and 10,000 hours) following the start of pumping. As expected, the water level exhibits a gradual decline over time. Notably, after 100 hours, the water level reaches a depth of 20 meters at the pumping location (0 m). Upon reaching a steady-state flow after 1000 hours, the water level stabilizes and shows no further change.

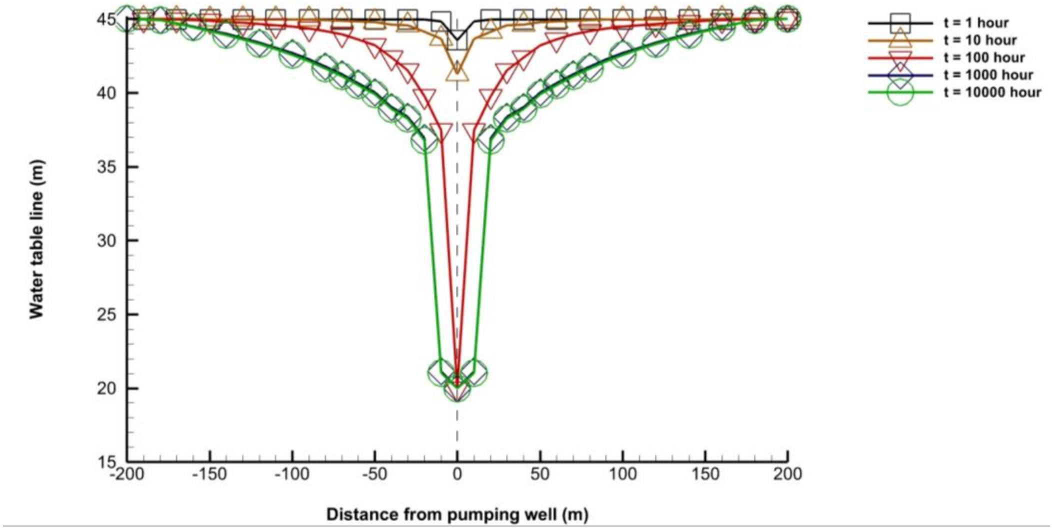

Fig 11 Water level drops relative to the impermeable bedrock at various distances from the pumping well and over various time periods

5. Parametric Analysis

To study the effects of various aquifer parameters such as hydraulic conductivity (due to material's permeability variation), elastic modulus, and Poisson's ratio on hydraulic head variation and land subsidence, we conduct parametric analyses considering isotropic conditions.

5.1. Hydraulic Conductivity

We investigate four different permeability values to assess how the aquifer's hydraulic conductivity affects land subsidence and variations in the hydraulic head. We assume that the viscosity and the specific weight of water do not change, so the change in hydraulic conductivity is only due to a change in the material's pore space. Figure 12 depicts hydraulic head variation in time at observation point HO for different hydraulic conductivity values. The influence of the aquifer's permeability on the system is more significant until a steady state is reached. Permeability has a minimal impact on the ultimate hydraulic head values in steady state, especially when the hydraulic conductivity is equal to or greater than a certain value, as in this case for values equal to or greater than $1K$.

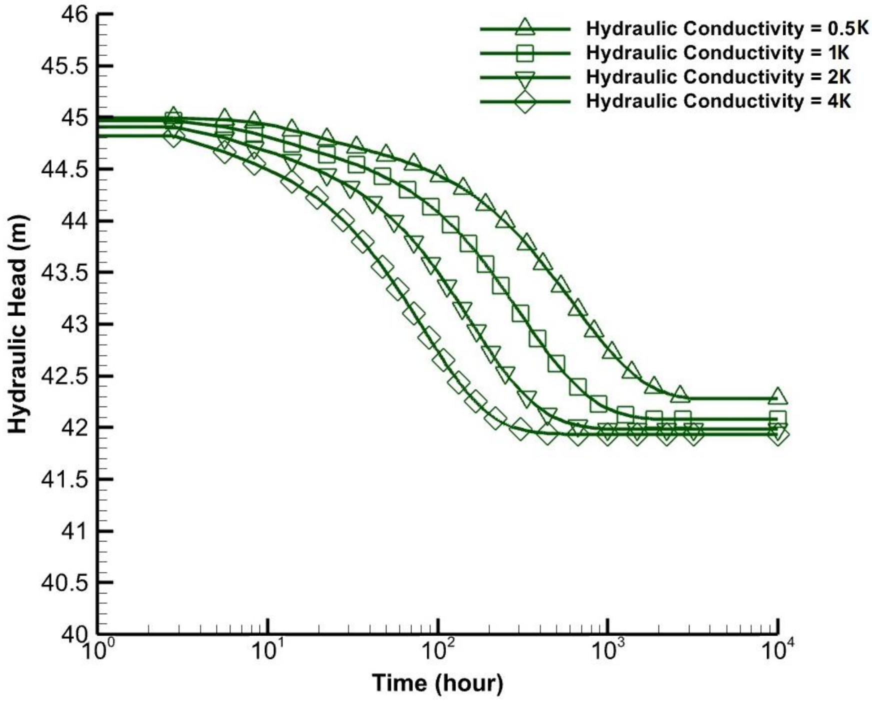

Fig 12. Hydraulic head variation over time for different hydraulic conductivity values $\left(1K = 3.65 \times 10^{-5}\,\frac{m}{s}\right)$

Figure 13 illustrates land subsidence over time for different hydraulic conductivity values at the observation point DO. We observe that changes in aquifer permeability do not significantly impact the ultimate subsidence values. Instead, higher hydraulic conductivity in the aquifer leads to subsidence within a shorter timeframe. Thus, similar to hydraulic conductivity, the effect of permeability is primarily seen during the timeframe in which subsidence occurs. Permeability minimally impacts the ultimate land subsidence values in steady state condition, especially when the hydraulic conductivity is equal to or greater than a certain value, as in this case for values equal to or greater than $1K$. It can be concluded that this parameter does not substantially influence the ultimate depth of subsidence.

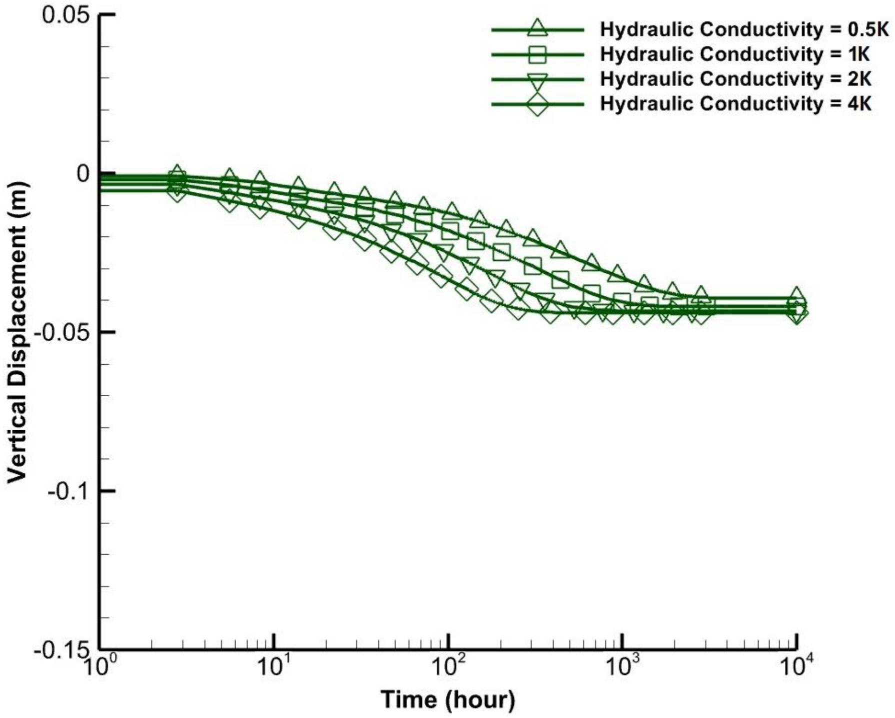

Fig 13 Land subsidence over time for different hydraulic conductivity values $\left(1K = 3.65 \times 10^{-5}\,\frac{m}{s}\right)$

5.2. Elastic Modulus

The study was repeated with changing elastic modulus values to examine their influence on the extent of land subsidence and the hydraulic head variations within the aquifer. Figure 14 demonstrates the effect of the aquifer's elastic modulus on the hydraulic head reduction at monitoring point HO. We observe that the aquifer's elastic modulus represents minimal impact on the downward trend of the hydraulic head. Under steady-state conditions, the hydraulic head remains consistent for different elastic modulus levels. Therefore, it can be concluded that the aquifer's elastic modulus has a negligible effect on the ultimate hydraulic head decrease.

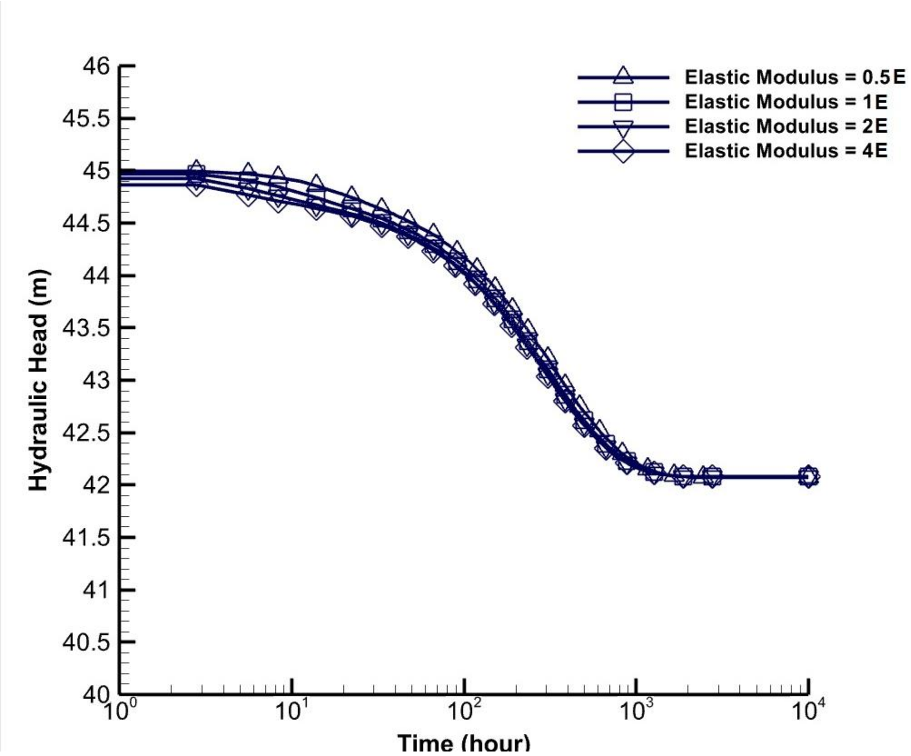

Fig 14 Hydraulic head variation over time for different elastic modulus values $(1E = 14.7\ GPa)$

Figure 15 shows the effect of the aquifer's elastic modulus on the land subsidence at observation point DO. We note that the elastic modulus parameter significantly influences the ultimate land subsidence. A substantial increase in land subsidence occurs when the aquifer's elastic modulus is halved $(0.5E)$. As elastic modulus doubles $(2E)$ and quadruples $(4E)$, the rate of decrease in the ultimate subsidence non-linearly decreases compared with $0.5E$ to E variation. In contrast to ultimate subsidence values, the time that renders steady state condition does not change for different elastic moduli. Based on the parametric study, obtaining precise elastic modulus measurements through meticulous field assessments or laboratory tests is crucial for land subsidence studies.

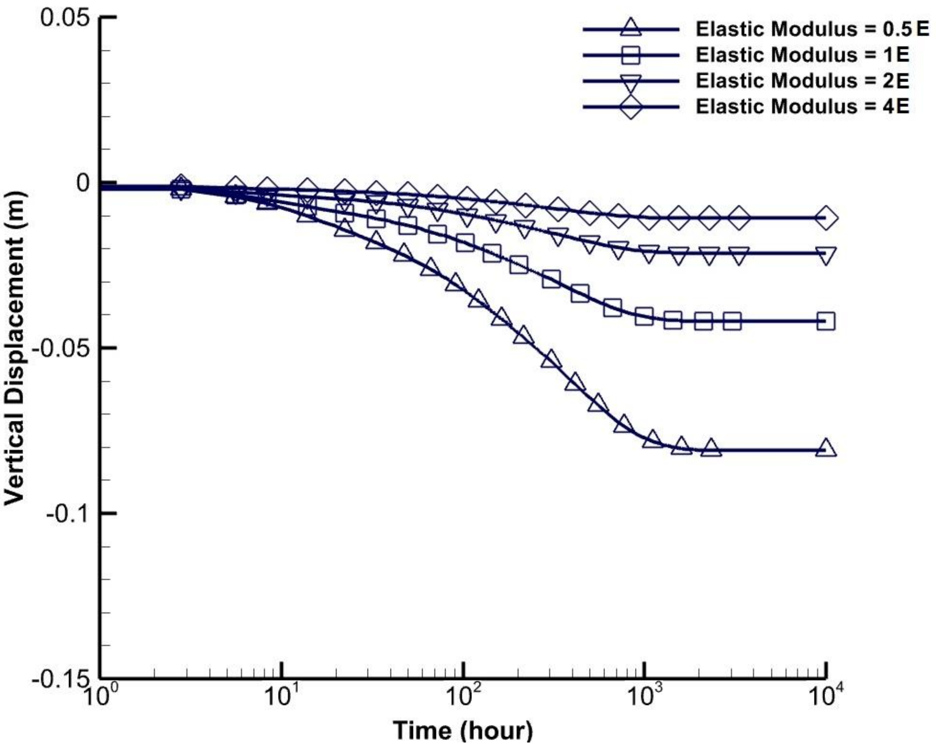

Fig 15 Land subsidence over time for different elastic modulus values $(1E = 14.7\ GPa)$

5.3. Poisson's Ratio

The impact of the aquifer's Poisson's ratio on hydraulic head change in time at observation point HO is shown in Figure 16. As we see, Poisson's ratio has a minimal effect on the hydraulic head trend and its ultimate value. This observation aligns with the fact that Poisson's ratio primarily influences the stress-strain relationship rather than directly affecting hydraulic properties, as illustrated by the governing equations discussed in subsection 2.1.

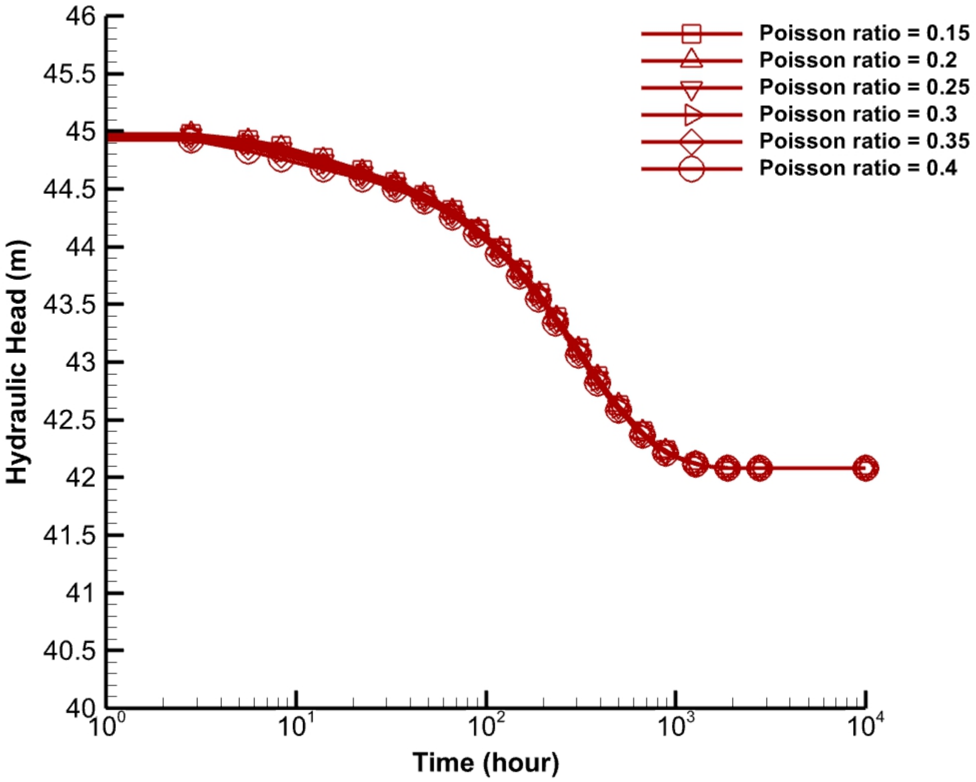

Fig 16 Hydraulic head variation over time for different Poisson's ratios

As shown in Figure 17, land subsidence at observation point DO decreases with the increasing Poisson's ratio. This observation is consistent with the correlation between bulk modulus and Poisson's ratio, $K = \frac{E}{3(1-2v)}$. Based on the inverse correlation between compressibility and bulk modulus, it can be inferred that when Poisson's ratio increased to the limiting value of 0.5, the compressibility of the model decreased. Therefore, as the ultimate land subsidence increases as Poisson's ratio decreases, it could be beneficial to measure Poisson's ratio with field evaluations or lab experiments for more informed research on land subsidence.

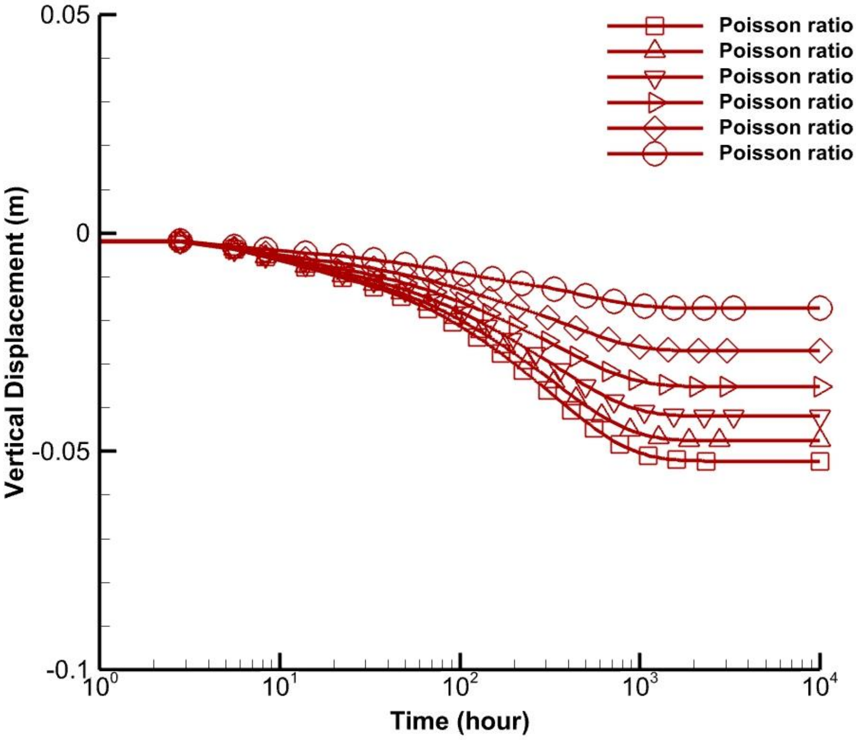

Fig 17 Land subsidence over time for different Poisson ratios

6. Conclusions

A series of hydraulic and coupled hydromechanical models were presented to validate the developed EFG code for flow and deformation analysis. The EFG model was validated first using a multiphase flow hydraulic benchmark problem and then, with an unsaturated hydromechanical consolidation benchmark problem. Analyzing the results obtained from the EFG model alongside theoretical results and outcomes from other computational algorithms highlights two essential aspects: 1) the EFG model is appropriately developed and formulated, and 2) it can provide precise and reliable solutions for soil deformation and fluid flow issues in evolving three-phase porous materials.

Upon establishing the validity of our EFG code, we proceeded to construct a model of an aquifer to: 1) investigate the process of three-dimensional groundwater flow and land deformation due to groundwater extraction from unsaturated geologic media, 2) evaluate the effects of true anisotropy on such a hydromechanical phenomenon, and 3) understand the effect of various characteristics of aquifers. The material properties for the true anisotropic and isotropic aquifers, essential for conducting numerical simulations, were obtained from existing literature. Results derived from numerical simulations underscore the significance of true anisotropy, which is influential in the context of the groundwater flow dynamic and the deformation of the solid skeletal structure.

The results of both isotropic and anisotropic scenarios highlight a nonlinear correlation between groundwater pumping and the subsequent decrease in hydraulic head and land subsidence augmentation in the unsaturated media. To ascertain the reliability of the modeling, we compared EFG results with FEM land subsidence and hydraulic head results. In the case of isotropic aquifers, the results from the EFG model on land subsidence and variations in hydraulic head exhibit a decent agreement in both trend and final values when compared with FEM outcomes. In the anisotropic aquifer scenario, EFG and FEM models display similar trends in land subsidence and reduction in the hydraulic head, and final land subsidence and hydraulic head values are closely aligned. However, a divergence is observed between EFG and FEM results during the initial hours of pumping. The FEM model demonstrates that nearly half of the total steady-state land subsidence occurs within the first hour of water extraction, a contrast to the isotropic model where vertical displacement alterations commence post a 6-hour pumping duration. In comparison, the EFG model suggests the onset of land subsidence in the anisotropic model after approximately 4 hours of pumping, showing greater agreement with the isotropic model than the FEM model. Nonetheless, while the FEM model indicates a consistent subsidence trend for both isotropic and anisotropic aquifers, the EFG model displays a variation. This disparity accentuates the necessity for further research, including the validation of EFG and FEM models with field data to verify the results in the early stages of pumping.

The parametric study indicates that the elastic modulus and Poisson's ratio exert the most pronounced influence on the extent of land subsidence. While hydraulic conductivity predominantly governs the rate of hydraulic decrease and the onset of land subsidence, its influence on the final values of hydraulic head and land subsidence at the steady-state condition is comparatively marginal. These observations underscore the importance of obtaining accurate in-situ measurements of the elastic modulus and Poisson's ratio for groundwater extraction initiatives, as these parameters are essential for ensuring the accuracy and reliability of feasibility studies in such projects.

Acknowledgments: We thank Dr. Soodeh Samimi for developing the initial version of the EFG software. Additionally, we appreciate the High-Performance Computing (HPC) center at Sharif University of Technology for providing computing resources.

Funding: This research received no external funding.

Author Contributions: Conceptualization, Ahmad Tourei, Ali Pak; Methodology: Ahmad Tourei, Ali Pak, Mohammadali Iranmanesh; Software: Ahmad Tourei, Mohammadali Iranmanesh, Mohammadreza Naddafnia; Formal analysis and investigation: Ahmad Tourei, Ali Pak; Visualization: Ahmad Tourei, Mohammadreza Naddafnia; Writing - original draft preparation: Ahmad Tourei, Mohammadreza Naddafnia; Writing - review and editing: Ahmad Tourei, Ali Pak, Mohammadali Iranmanesh, Mohammadreza Naddafnia; Resources: Ahmad Tourei, Ali Pak; Supervision: Ali Pak,

Code Availability Statement: Some or all data, models, or codes that support the findings of this study are available from the corresponding author upon reasonable request.

Competing Interests: The authors declare no conflict of interest and disclose any financial interests.

Disclaimer: Every author has reviewed and provided feedback on earlier drafts of this manuscript, as well as read and given their approval for the current version, with all agreeing to be listed as coauthors. Furthermore, the authors affirm that the manuscript submitted is original, has not been published elsewhere, and is not currently being considered for publication elsewhere.

Appendix A

Within the local coordinates (x', y', z'), along which the principal axes of an anisotropic (orthotropic) geological medium are aligned, the generalized Hooke's law can be represented in vector form as described by (Kim, 2005; Love, 1944)

$$\sigma'^{eL} = D^L \varepsilon^L \tag{A1}$$

where $\sigma'^{eL} = \left\{\sigma'^{e}_{x'x'}\ \sigma'^{e}_{y'y'}\ \sigma'^{e}_{z'z'}\ \sigma'^{e}_{x'y'}\ \sigma'^{e}_{y'z'}\ \sigma'^{e}_{z'x'}\right\}^T$, represents the local incremental effective stress vector, D^L is the local elastic modulus tensor, and $\varepsilon^L = \left\{\varepsilon_{x'x'}\ \varepsilon_{y'y'}\ \varepsilon_{z'z'}\ \varepsilon_{x'y'}\ \varepsilon_{y'z'}\ \varepsilon_{z'x'}\right\}^T$ is the local strain vector. The local elastic modulus tensor D^L is then defined using $\frac{v_{ij}}{E_i} = \frac{v_{ij}}{E_j}$ for $i, j = x', y', z'$ as follows:

$$D^L = \begin{bmatrix} D^L_{11} & D^L_{12} & D^L_{13} & 0 & 0 & 0 \\ D^L_{21} & D^L_{22} & D^L_{23} & 0 & 0 & 0 \\ D^L_{31} & D^L_{32} & D^L_{33} & 0 & 0 & 0 \\ 0 & 0 & 0 & D^L_{44} & 0 & 0 \\ 0 & 0 & 0 & 0 & D^L_{55} & 0 \\ 0 & 0 & 0 & 0 & 0 & D^L_{66} \end{bmatrix} \tag{A2}$$

and

$$D^L_{11} = \left(\frac{1}{E_{y'}E_{z'}} - \frac{v^2_{y'z'}}{E^2_{y'}}\right)|C^L|^{-1} \tag{A3}$$

$$D^L_{12} = D^L_{21} = \left(\frac{v_{x'y'}}{E_{x'}E_{z'}} + \frac{v_{x'z'}v_{y'z'}}{E_{x'}E_{y'}}\right)|C^L|^{-1} \tag{A4}$$

$$D^L_{13} = D^L_{31} = \left(\frac{v_{x'y'}}{E_{x'}E_{y'}} + \frac{v_{x'y'}v_{y'z'}}{E_{x'}E_{y'}}\right)|C^L|^{-1} \tag{A5}$$

$$D^L_{22} = \left(\frac{1}{E_{x'}E_{z'}} - \frac{v^2_{x'z'}}{E^2_{x'}}\right)|C^L|^{-1} \tag{A6}$$

$$D^L_{23} = D^L_{32} = \left(\frac{v_{x'y'}v_{x'z'}}{E^2_{x'}} + \frac{v_{y'z'}}{E_{x'}E_{y'}}\right)|C^L|^{-1} \tag{A7}$$

$$D^L_{33} = \left(\frac{1}{E_{x'}E_{y'}} - \frac{v^2_{x'y'}}{E^2_{x'}}\right)|C^L|^{-1} \tag{A8}$$

$$D^L_{44} = G_{x'y'} \tag{A9}$$

$$D^L_{55} = G_{y'z'} \tag{A10}$$

$$D^L_{66} = G_{z'x'} \tag{A11}$$

$$|C^L| = \frac{1}{E_{x'}E_{y'}E_{z'}} - \frac{v^2_{x'y'}}{E^2_{x'}E_{y'}} - \frac{v^2_{y'z'}}{E^2_{y'}E_{x'}} - \frac{v^2_{x'z'}}{E^2_{x'}E_{y'}} - \frac{2v_{x'y'}v_{x'z'}v_{y'z'}}{E^2_{x'}E_{y'}} \tag{A12}$$

where $|C^L|$ is the determinant of the local elastic compliance tensor $C^L_{ijkl} = C^L = D^{L^{-1}}$, E_i is elastic modulus in the i direction, v_{ij} is Poisson's ratio for normal strain in the j direction due to effective normal stress in the i direction, G_{ij} is the shear modulus in the ij plane, only nine terms are required. In a cross-anisotropic (transversely isotropic) geological medium concerning the local z' axis, $v_{x'y'} \neq v_{y'z'} = v_{x'z'}, E_{x'} = E_{y'} \neq E_{z'}, G_{x'y'} \neq G_{y'z'} = G_{z'x'}$, and $G_{x'y'} = \frac{E_{x'}}{2(1+v_{x'y'})}$ thus only five terms are necessary. In an isotropic geological medium, $v = v_{x'y'} = v_{y'z'} = v_{x'z'}, E = E_{x'} = E_{y'} = E_{z'}, G = G_{x'y'} = G_{y'z'} = G_{z'x'}$, and $G = \frac{E}{2(1+v)}$, hence, only two terms are needed. The generalized Hooke's law for the anisotropic (orthotropic) geological medium in global coordinates (x, y, z), represented by equation (2b), can also be expressed in vector form using engineering notations, according to (Love, 1944):

$$\sigma'^{e} = D\varepsilon \tag{A13}$$

where $\sigma'^{e} = \{\sigma'^{e}_{xx}\sigma'^{e}_{yy}\sigma'^{e}_{zz}\sigma'^{e}_{xy}\sigma'^{e}_{yz}\sigma'^{e}_{zx}\}^{T}$represents the global incremental effective stress vector, D is the global elastic modulus (stiffness) tensor, and $\varepsilon = \{\varepsilon_{xx}\varepsilon_{yy}\varepsilon_{zz}\varepsilon_{xy}\varepsilon_{yz}\varepsilon_{zx}\}^{T}$ is the global strain vector. The definition of the global elastic modulus tensor D is as follows:

$$D = \begin{bmatrix} D_{11} & D_{12} & D_{13} & D_{14} & D_{15} & D_{16} \\ D_{21} & D_{22} & D_{23} & D_{24} & D_{25} & D_{26} \\ D_{31} & D_{32} & D_{33} & D_{34} & D_{35} & D_{36} \\ D_{41} & D_{42} & D_{43} & D_{44} & D_{45} & D_{46} \\ D_{51} & D_{52} & D_{53} & D_{54} & D_{55} & D_{56} \\ D_{61} & D_{62} & D_{63} & D_{64} & D_{65} & D_{66} \end{bmatrix} \tag{A14}$$

In Equation B14, $D_{ab} = D_{ba}$ for $a, b = 1,2,3,4,5,6$, a total of 21 terms needs to be computed. The calculation of the global elastic modulus tensor D can be derived from the local elastic modulus tensor D^{L} using a coordinate transformation matrix B as outlined by (Clebsch, 1994):

$$D = B^{T}D^{L}B \tag{A15}$$

and,

$$B = \begin{bmatrix} l_{x'}^{2} & m_{x'}^{2} & n_{x'}^{2} & l_{x'}m_{x'} & m_{x'}n_{x'} & n_{x'}l_{x'} \\ l_{y'}^{2} & m_{y'}^{2} & n_{y'}^{2} & l_{y'}m_{y'} & m_{y'}n_{y'} & n_{y'}l_{y'} \\ l_{z'}^{2} & m_{z'}^{2} & n_{z'}^{2} & l_{z'}m_{z'} & m_{z'}n_{z'} & n_{z'}l_{z'} \\ 2l_{x'}l_{y'} & 2m_{x'}m_{y'} & 2n_{x'}n_{y'} & l_{x'}m_{y'} + l_{y'}m_{x'} & m_{x'}n_{y'} + m_{y'}n_{x'} & n_{x'}l_{y'} + n_{y'}l_{x'} \\ 2l_{y'}l_{z'} & 2m_{y'}m_{z'} & 2n_{y'}n_{z'} & l_{y'}m_{z'} + l_{z'}m_{y'} & m_{y'}n_{z'} + m_{z'}n_{y'} & n_{y'}l_{z'} + n_{z'}l_{y'} \\ 2l_{z'}l_{x'} & 2m_{z'}m_{x'} & 2n_{z'}n_{x'} & l_{z'}m_{x'} + l_{x'}m_{z'} & m_{z'}n_{x'} + m_{x'}n_{z'} & n_{z'}l_{x'} + n_{x'}l_{z'} \end{bmatrix} \tag{A16}$$

The determination of the 36 terms within the coordinate transformation matrix B can be achieved by utilizing the nine terms from the coordinate transformation matrix A,

$$A = \begin{pmatrix} l_{x'} & m_{x'} & n_{x'} \\ l_{y'} & m_{y'} & n_{y'} \\ l_{z'} & m_{z'} & n_{y'} \end{pmatrix} \tag{A17}$$

The nine elements within the coordinate transformation matrix A correspond to the directional cosines between the local coordinates (x', y', z') and the global coordinates (x, y, z). In this context, l, m, and n represent x, y, and z , respectively.

Appendix B

The generalized Darcy's law can be indicated in a vector form in the local coordinates (x', y', z') which are aligned with the principal axes (i.e., principal directions) of an anisotropic (orthotropic) geologic medium (Kim, 2005):

$$q_{r}^{L} = -K_{r}K_{sat}^{L} \cdot \nabla_{\emptyset}^{L} \tag{B1}$$

where $q_{r}^{L} = \{q_{rx'}, q_{ry'}, q_{rz'}\}$ is the local Darcy flux, K_{sat}^{L} is the saturated hydraulic conductivity tensor, and $\nabla_{\emptyset}^{L} = \left\{\partial\emptyset\frac{}{\partial x'}\ \partial\emptyset\frac{}{\partial y'}\ \partial\emptyset\frac{}{\partial z'}\right\}^{T}$ is the hydraulic gradient. Besides, the local saturated hydraulic conductivity tensor K_{sat}^{L} defined as:

$$K_{sat}^{L} = \begin{pmatrix} K_{sat\,x'x'} & 0 & 0 \\ 0 & K_{sat\,y'y'} & 0 \\ 0 & 0 & K_{sat\,z'z'} \end{pmatrix} \tag{B2}$$

In the anisotropic geological medium $K_{sat\,x'x'} \neq K_{sat\,y'y'} \neq K_{sat\,z'z'}$, and therefore, only three terms should be given. In a cross-anisotropic (transversely isotropic) geological medium with respect to the local z' axis, $K_{sat\,x'x'} = K_{sat\,y'y'} \neq K_{sat\,z'z'}$, and thus, only two terms are needed. In an isotropic geological medium, $K_{sat}=K_{sat\,x'x'}=K_{sat\,y'y'}=K_{sat\,z'z'}$, and only one term is required. The generalized Darcy's law for the anisotropic geological medium in global coordinates (x,y,z), represented by equation (1), can also be expressed as a vector as follows:

$$q_r=-K_rK_{sat}\cdot\nabla_{\emptyset} \tag{B3}$$

where $q_r=\left\{q_{r\,x}\;q_{r\,y}\;q_{r\,z}\right\}^T$ represents the global Darcy flux, $\nabla_{\emptyset}=\left\{\partial\emptyset\frac{}{\partial x}\;\partial\emptyset\frac{}{\partial y}\;\;\partial\emptyset\frac{}{\partial z}\right\}^T$ is the global hydraulic gradient, and K_{sat} is the tensor for global saturated hydraulic conductivity:

$$K_{sat}=\begin{pmatrix}K_{sat\,xx} & K_{sat\,xy} & K_{sat\,xz}\\ K_{sat\,yx} & K_{sat\,yy} & K_{sat\,yz}\\ K_{sat\,zx} & K_{sat\,zy} & K_{sat\,zz}\end{pmatrix} \tag{B4}$$

where $K_{sat\,ij}=K_{sat\,ji}$ for $i,j=x,y,z$, six terms need to be computed. The calculation of the global saturated hydraulic conductivity tensor K_{sat} can be derived from the local saturated hydraulic conductivity tensor K_{sat}^L through a coordinate transformation matrix A as outlined in (Clebsch, 1994):

$$K_{sat}=A^TK_{sat}^LA \tag{B5}$$

The nine elements within the coordinate transformation matrix A correspond to the directional cosines between the local coordinates and the global coordinates as detailed in Appendix A (refer to equation (A17)).

Appendix C

The nodal matrices and vectors in Equations 9 and 10 are defined as (Samimi & Pak, 2016):

$$C_{11\,IJ}=\int_{\Omega}B_I^TD_TB_Jd\Omega \tag{C1}$$

$$C_{u\,IJ}^{\alpha}=\int_{\Gamma_u}\phi_I^T\alpha_{p_u}\phi_Jd\Gamma \tag{C2}$$

$$C_{12\,IJ}=\int_{\Omega}B_I^T\alpha m\left(s_w+\frac{\partial s_w}{\partial p_c}p_c\right)\phi_Jd\Omega \tag{C3}$$

$$C_{13\,IJ}=\int_{\Omega}B_I^T\alpha m\left((1-s_w)-\frac{\partial s_w}{\partial p_c}p_c\right)\phi_Jd\Omega \tag{C4}$$

$$F_{u\,I}=\int_{\Omega}\phi_I^T\rho gd\Omega+\int_{\Gamma_t}\phi_I^T\bar{t}d\Gamma \tag{C5}$$

$$F_{uI}^{\alpha}=\int_{\Gamma_u}\phi_I^T\alpha_{pu}\bar{u}d\Gamma \tag{C6}$$

$$C_{21\,IJ}=\int_{\Omega}\phi_I\alpha s_wm^TB_Jd\Omega \tag{C7}$$

$$C_{22\,IJ}=\int_{\Omega}\phi_I\left[s_w\frac{\alpha-n}{K_s}\left(s_w+\frac{\partial s_w}{\partial p_c}p_c\right)-n\frac{\partial s_w}{\partial p_c}+n\frac{s_w}{k_w}\right]\phi_Jd\Omega \tag{C8}$$

$$C_{23\,IJ}=\int_{\Omega}\phi_I\left[s_w\frac{\alpha-n}{K_s}\left(1-s_w-\frac{\partial s_w}{\partial p_c}p_c\right)+n\frac{\partial s_w}{\partial p_c}\right]\phi_Jd\Omega \tag{C9}$$

$$K_{22\,IJ}=\int_{\Omega}B_{pI}^T\frac{kk_{rw}}{\mu_w}B_{pJ}d\Omega \tag{C10}$$

$$K_{pw\,IJ}^{\alpha}=\int_{\Gamma_{pw}}\phi_I\alpha_{p_{pw}}\phi_Jd\Gamma \tag{C11}$$

$$F_{pw\,I} = \int_{\Omega} B_{pI}^{T} \frac{kk_{rw}}{\mu_w} \rho_w g d\Omega - \int_{\Gamma_{qw}} \phi_I \bar{q}_w d\Gamma \tag{C12}$$

$$F_{pw\,I}^{\alpha} = \int_{\Gamma_{pw}} \phi_I\, \alpha_{p_{pw}} \bar{p}_w d\Gamma \tag{C13}$$

$$C_{31IJ} = \int_{\Omega} \phi_I \alpha (1 - s_w) m^T B_J d\Omega \tag{C14}$$

$$C_{32\,IJ} = \int_{\Omega} \phi_I \left[(1 - s_w) \frac{\alpha - n}{K_s} (s_w + \frac{\partial s_w}{\partial p_c} p_c) + n \frac{\partial s_w}{\partial p_c} \right] \phi_J d\Omega \tag{C15}$$

$$C_{33\,IJ} = \int_{\Omega} \phi_I \left[(1 - s_w) \frac{\alpha - n}{K_s} (1 - s_w - \frac{\partial s_w}{\partial p_c} p_c) + n \frac{1 - s_w}{K_{nw}} - n \frac{\partial s_w}{\partial p_c} \right] \phi_J d\Omega \tag{C16}$$

$$K_{33\,IJ} = \int_{\Omega} B_{pI}^{T} \frac{kk_{rnw}}{\mu_{nw}} B_{pJ} d\Omega \tag{C17}$$

$$K_{pnw\,IJ}^{\alpha} = \int_{\Gamma_{pmr}} \phi_I \alpha_{p_{pmw}} \phi_J d\Gamma \tag{C18}$$

$$F_{pnw\,I} = \int_{\Omega} B_{pI}^{T} \frac{kk_{nw}}{\mu_{nw}} \rho_{nw} g d\Omega - \int_{\Gamma_{qnw}} \phi_I \bar{q}_{nw} d\Gamma \tag{C19}$$

$$F_{pnw\,I}^{\alpha} = \int_{\Gamma_{pnw}} \phi_I \alpha_{p_{pnw}} \bar{p}_{nw} d\Gamma \tag{C20}$$

where $m = [\,1, 1, 1, 0, 0, 0]^T$

References

Abidin, H. Z., Djaja, R., Rais, J., & Wedyanto, K. (2004). Land Subsidence of Jakarta Metropolitan Area. *FIPG Regional Conference*, *III*(December).

Amir Hosseini, M., Kamrava, S., Sahimi, M., & Tahmasebi, P. (2023). Effect of Wettability on Two-Phase Flow Through Granular Porous Media: Fluid Rupture and Mechanics of the Media. *Chemical Engineering Science*, *269*. https://doi.org/10.1016/j.ces.2023.118446

Asadi, R., & Ataie-Ashtiani, B. (2015). A comparison of finite volume formulations and coupling strategies for two-phase flow in deforming porous media. *Computers and Geotechnics*, *67*. https://doi.org/10.1016/j.compgeo.2015.02.004

Asadizadeh, M., Khosravi, S., Karimi, J., Sherizadeh, T., Vajedian, S., & Hossaini, M. F. (2022). Mechanical behavior of single-flawed cylindrical specimens subjected to axial loading: a numerical investigation. *Bulletin of Engineering Geology and the Environment*, *81*(10). https://doi.org/10.1007/s10064-022-02940-4

Bell, J. W., Amelung, F., Ramelli, A. R., & Blewitt, G. (2002). Land subsidence in Las Vegas, Nevada, 1935-2000: New geodetic data show evolution, revised spatial patterns and reduced rates. *Environmental and Engineering Geoscience*, *8*(3). https://doi.org/10.2113/8.3.155

Belytschko, T., Lu, Y. Y., & Gu, L. (1994). Element-free Galerkin methods. *International Journal for Numerical Methods in Engineering*, *37*(2), 229–256. https://doi.org/10.1002/nme.1620370205

Bonì, R., Herrera, G., Meisina, C., Notti, D., Béjar-Pizarro, M., Zucca, F., González, P. J., Palano, M., Tomás, R., Fernández, J., Fernández-Merodo, J. A., Mulas, J., Aragón, R., Guardiola-Albert, C., & Mora, O. (2015). Twenty-year advanced DInSAR analysis of severe land subsidence: The Alto Guadalentín Basin (Spain) case study. *Engineering Geology*, *198*. https://doi.org/10.1016/j.enggeo.2015.08.014

Brooks, R., & Corey, A. (1964). Hydraulic properties of porous media. *Hydrology Papers, Colorado State University*, *3*(March), 37 pp. http://www.citeulike.org/group/1336/article/711012

Callari, C., & Abati, A. (2009). Finite element methods for unsaturated porous solids and their application to dam engineering problems. *Computers and Structures*, *87*(7–8), 485–501. https://doi.org/10.1016/j.compstruc.2008.12.012

Celia, M. A., & Binning, P. (1992). A mass conservative numerical solution for two-phase flow in porous media with application to unsaturated flow. *Water Resources Research*, *28*(10). https://doi.org/10.1029/92WR01488

Chai, J. C., Shen, S. L., Zhu, H. H., & Zhang, X. L. (2004). Land subsidence due to groundwater drawdown in Shanghai. *Geotechnique*, *54*(2). https://doi.org/10.1680/geot.2004.54.2.143

Clebsch, A. (1994). Selected contributions to groundwater hydrology by C.V. Theis, and a review of his life and work. *US Geological Survey Water-Supply Paper*, *2415*.

Dinesh, P., Ranjith, P. G., Behera, M. R., & Muthu, N. (2021). Experimental and numerical (EFG method) studies on sedimentary rock under varied salinity conditions. *International Journal of Rock Mechanics and Mining Sciences*, *148*, 104909. https://doi.org/10.1016/J.IJRMMS.2021.104909

Donoso, M., Di Baldassarre, G., Boegh, E., Browning, A., Oki, T., Tindimugaya, C., Vairavamoorthy, K., Vrba, J., Zalewski, M., & Zubari, W. K. (2012). *International Hydrological Programme (IHP) eighth phase: Water security: responses to local, regional and global challenges. Strategic plan, IHP-VIII (2014-2021)*. http://unesdoc.unesco.org/images/0021/002180/218061e.pdf

El Kamali, M., Papoutsis, I., Loupasakis, C., Abuelgasim, A., Omari, K., & Kontoes, C. (2021). Monitoring of land surface subsidence using persistent scatterer interferometry techniques and ground truth data in arid and semi-arid regions, the case of Remah, UAE. *Science of the Total Environment*, *776*. https://doi.org/10.1016/j.scitotenv.2021.145946

Fulton, A. (2006). Land subsidence: What is it and why is it an important aspects of groundwater management. *Sacramento: California Department of Water Resources*.

Galloway, D. L., & Burbey, T. J. (2011). Review: Regional land subsidence accompanying groundwater extraction. *Hydrogeology Journal*, *19*(8). https://doi.org/10.1007/s10040-011-0775-5

Ghazifard, A., Moslehi, A., Safaei, H., & Roostaei, M. (2016). Effects of groundwater withdrawal on land subsidence in Kashan Plain, Iran. *Bulletin of Engineering Geology and the Environment*, *75*(3). https://doi.org/10.1007/s10064-016-0885-3

Hu, B., Chen, X., & Zhang, X. (2019). Using multisensor SAR datasets to monitor land subsidence in Los Angeles from 2003 to 2017. *Journal of Sensors*, *2019*. https://doi.org/10.1155/2019/9389820

Imakiire, T., & Koarai, M. (2012). Wide-area land subsidence caused by "the 2011 off the Pacific Coast of Tohoku Earthquake." *Soils and Foundations*, *52*(5). https://doi.org/10.1016/j.sandf.2012.11.007

Iranmanesh, M. A., & Pak, A. (2023). Three-dimensional numerical simulation of hydraulically driven cohesive fracture propagation in deformable reservoir rock using enriched EFG method. *Computational Geosciences*, *27*(2), 317–335. https://doi.org/10.1007/S10596-023-10198-2/METRICS

Iranmanesh, M. A., Pak, A., & Samimi, S. (2018). Non-isothermal simulation of the behavior of unsaturated soils using a novel EFG-based three dimensional model. *Computers and Geotechnics*, *99*, 93–103. https://doi.org/10.1016/j.compgeo.2018.02.024

Khoei, A. R., & Mohammadnejad, T. (2011). Numerical modeling of multiphase fluid flow in deforming porous media: A comparison between two- and three-phase models for seismic analysis of earth and rockfill dams. *Computers and Geotechnics*, *38*(2), 142–166. https://doi.org/10.1016/j.compgeo.2010.10.010

Khorrami, M., Abrishami, S., Maghsoudi, Y., Alizadeh, B., & Perissin, D. (2020). Extreme subsidence in a populated city (Mashhad) detected by PSInSAR considering groundwater withdrawal and geotechnical properties. *Scientific Reports*, *10*(1). https://doi.org/10.1038/s41598-020-67989-1

Khorrami, M., Shirzaei, M., Ghobadi-Far, K., Werth, S., Carlson, G., & Zhai, G. (2023). Groundwater Volume Loss in Mexico City Constrained by InSAR and GRACE Observations and Mechanical Models. *Geophysical Research Letters*, *50*(5). https://doi.org/10.1029/2022GL101962

Kihm, J. H., Kim, J. M., Song, S. H., & Lee, G. S. (2007). Three-dimensional numerical simulation of fully coupled groundwater flow and land deformation due to groundwater pumping in an unsaturated fluvial aquifer system. *Journal of Hydrology*, *335*(1–2), 1–14. https://doi.org/10.1016/j.jhydrol.2006.09.031

Kim, J. M. (2005). Three-dimensional numerical simulation of fully coupled groundwater flow and land deformation in unsaturated true anisotropic aquifers due to groundwater pumping. *Water Resources Research*, *41*(1), 1–16. https://doi.org/10.1029/2003WR002941

Lehmann, F., & Ackerer, P. (1998). Comparison of iterative methods for improved solutions of the fluid flow equation in partially saturated porous media. *Transport in Porous Media*, *31*(1–3).

Love, A. E. H. (1944). A Treatise on the Mathematical Theory of Elasticity, fourth ed. *In: Dislocations in Solids*.

Luo, Z. J., & Zeng, F. (2011). Finite element numerical simulation of land subsidence and groundwater exploitation based on visco-elastic-plastic Biot's consolidation theory. *Journal of Hydrodynamics*, *23*(5). https://doi.org/10.1016/S1001-6058(10)60157-6

Mohammadi, M. G. and S. (2006). Weak discontinuity in porous media: an enriched EFG method for fully coupled layered porous media. *International Journal for Numerical and Analytical Methods in Geomechanics*, *30*(13), 1303–1336. https://doi.org/10.1002/nag

Motagh, M., Djamour, Y., Walter, T. R., Wetzel, H. U., Zschau, J., & Arabi, S. (2007). Land subsidence in Mashhad Valley, northeast Iran: Results from InSAR, levelling and GPS. *Geophysical Journal International*, *168*(2), 518–526. https://doi.org/10.1111/j.1365-246X.2006.03246.x

Mousavi, S. M., Shamsai, A., El Naggar, M. H., & Khamehchian, M. (2001). A GPS-based monitoring program of land subsidence due to groundwater withdrawal in Iran. *Canadian Journal of Civil Engineering*, *28*(3), 452–464. https://doi.org/10.1139/cjce-28-3-452

Ohenhen, L. O., & Shirzaei, M. (2022). Land Subsidence Hazard and Building Collapse Risk in the Coastal City of Lagos, West Africa. *Earth's Future*, *10*(12). https://doi.org/10.1029/2022EF003219

Oliaei, M. N., Soga, K., & Pak, A. (2009). Some numerical issues using element-free Galerkin mesh-less method for coupled hydromechanical problems. *International Journal for Numerical and Analytical Methods in Geomechanics*, *33*(7). https://doi.org/10.1002/nag.747

Park, Y.-C., & Leap, D. I. (2000). Modeling groundwater flow by the element-free Galerkin (EFG) method. *Geosciences Journal*, *4*(3). https://doi.org/10.1007/bf02910141

Pathania, T., Bottacin-Busolin, A., Rastogi, A. K., & Eldho, T. I. (2019). Simulation of Groundwater Flow in an Unconfined Sloping Aquifer Using the Element-Free Galerkin Method. *Water Resources Management*, *33*(8). https://doi.org/10.1007/s11269-019-02261-4

Pathania, T., Eldho, T. I., & Bottacin-Busolin, A. (2020). Coupled simulation of groundwater flow and multispecies reactive transport in an unconfined aquifer using the element-free Galerkin method. *Engineering Analysis with Boundary Elements*, *121*, 31–49. https://doi.org/10.1016/j.enganabound.2020.08.019

Pathania, T., & Rastogi, A. K. (2017). Groundwater Flow Simulation in Confined Aquifer by Meshless Element Free Galerkin Method. *European Water*, *57*(2000), 505–512.

Philip, J. R. (1956). The Theory of Infiltration: 1. The Infiltration Equation and Its Solution. *Commonwealth Scientific and Industrial Research Organization*.

Poland, J. F., & Davis, G. H. (1969). Land Subsidence Due to Withdrawal of Fluids. In *Reviews in Engineering Geology* (pp. 187–269). Geological Society of America. https://doi.org/https://doi.org/10.1130/REG2

P.S. HUYAKORN, A. S. D. T. (2007). Techniques for Making Finite Elements Competitve in Modeling Flow in Variably Saturated Porous Media. *WATER RESOURCES RESEARCH*, *20*(8), 2–4.

Rahman, N. A., & Lewis, R. W. (1999). Finite element modelling of multiphase immiscible flow in deforming porous media for subsurface systems. *Computers and Geotechnics*, *24*(1), 41–63. https://doi.org/10.1016/S0266-352X(98)00029-9

Rajabi, A. M. (2018). A numerical study on land subsidence due to extensive overexploitation of groundwater in Aliabad plain, Qom-Iran. *Natural Hazards*, *93*(2), 1085–1103. https://doi.org/10.1007/s11069-018-3448-z

Samimi, S., & Pak, A. (2012). Three-dimensional simulation of fully coupled hydromechanical behavior of saturated porous media using Element Free Galerkin (EFG) method. *Computers and Geotechnics*, *46*. https://doi.org/10.1016/j.compgeo.2012.06.004

Samimi, S., & Pak, A. (2014). A novel three-dimensional element free Galerkin (EFG) code for simulating two-phase fluid flow in porous materials. *Engineering Analysis with Boundary Elements*, *39*(1). https://doi.org/10.1016/j.enganabound.2013.10.011

Samimi, S., & Pak, A. (2016). A three-dimensional mesh-free model for analyzing multi-phase flow in deforming porous media. *Meccanica*, *51*(3). https://doi.org/10.1007/s11012-015-0231-z

Shirzaei, M., Freymueller, J., Törnqvist, T. E., Galloway, D. L., Dura, T., & Minderhoud, P. S. J. (2021). Measuring, modelling and projecting coastal land subsidence. In *Nature Reviews Earth and Environment* (Vol. 2, Issue 1, pp. 40–58). Springer Nature. https://doi.org/10.1038/s43017-020-00115-x

Siade, A. J., Nishikawa, T., Rewis, D. L., Martin, P., & Phillips, S. P. (2014). Groundwater-flow and land-subsidence model of Antelope Valley, California. *Scientific Investigations Report*.

Tey, W. Y., Asako, Y., Ng, K. C., & Lam, W. H. (2020). A review on development and applications of element-free galerkin methods in computational fluid dynamics. *Https://Doi.Org/10.1080/15502287.2020.1821126*, *21*(5), 252–275. https://doi.org/10.1080/15502287.2020.1821126

Thomas, H. R. (2000). The Finite Element Method in the Static and Dynamic Deformation and Consolidation of Porous Media, 2nd edn, R. W. Lewis And B. A. Schrefler, Wiley, New York. *International Journal for Numerical and Analytical Methods in Geomechanics*, *24*(14). https://doi.org/10.1002/1096-9853(20001210)24:14<1107::aid-nag95>3.3.co;2-o

Tiwari, A., Narayan, A. B., Dwivedi, R., Swadeshi, A., Pasari, S., & Dikshit, O. (2020). Geodetic investigation of landslides and land subsidence: case study of the Bhurkunda coal mines and the Sirobagarh landslide. *Survey Review*, *52*(371). https://doi.org/10.1080/00396265.2018.1531654

Tourei, A., Pak, A., & Iranmanesh, M. A. (2024). Numerical modeling of land subsidence induced by groundwater extraction considering unsaturated effects and using element-free Galerkin (EFG) method. *Sharif Journal of Civil Engineering*. https://doi.org/10.24200/j30.2023.59625.3256

van Genuchten, M. Th. (1980). A Closed-form Equation for Predicting the Hydraulic Conductivity of Unsaturated Soils. *Soil Science Society of America Journal*, *44*(5), 892–898. https://doi.org/10.2136/sssaj1980.03615995004400050002x

Varshney, V., Chandra, S., & Bordas, S. (2020). Element-free galerkin method for reinforced timoshenko beam on elastic foundation. In *Lecture Notes in Civil Engineering* (Vol. 55). https://doi.org/10.1007/978-981-15-0886-8_52

Wang, Y. Q., Wang, Z. F., & Cheng, W. C. (2019). A review on land subsidence caused by groundwater withdrawal in Xi'an, China. *Bulletin of Engineering Geology and the Environment*, *78*(4), 2851–2863. https://doi.org/10.1007/s10064-018-1278-6

Xu, Y. S., Shen, S. L., Cai, Z. Y., & Zhou, G. Y. (2008). The state of land subsidence and prediction approaches due to groundwater withdrawal in China. *Natural Hazards*, *45*(1). https://doi.org/10.1007/s11069-007-9168-4

Yang, Y., Song, X. F., Zheng, F. D., Liu, L. C., & Qiao, X. J. (2015). Simulation of fully coupled finite element analysis of nonlinear hydraulic properties in land subsidence due to groundwater pumping. *Environmental Earth Sciences*, *73*(8). https://doi.org/10.1007/s12665-014-3705-8